11-5-2009

Thermal conductivity measurement of gas diffusion layer used in PEMFC

Arjun Radhakrishnan

Thermal Conductivity Measurement of Gas Diffusion Layer Used in PEMFC

by

Arjun Radhakrishnan

A Thesis Submitted in Partial Fulfillment of the Requirements

for the Degree of Master of Science

in Mechanical Engineering

Approved by:

Dr. Satish G. Kandlikar _____

Department of Mechanical Engineering (Thesis Advisor)

Dr. Tuhin K. Das _____

Department of Mechanical Engineering

Dr. Robert Stevens _____

Department of Mechanical Engineering

Dr. Edward C. Hensel _____

Department Head of Mechanical Engineering

Department of Mechanical Engineering

Kate Gleason College of Engineering

Rochester Institute of Technology

Rochester, NY

November 5, 2009

ABSTRACT

The objective of the present work is to develop an apparatus to measure the thermal conductivity of gas diffusion layer (GDL) as a function of temperature and compression, and also to develop an effective thermal conductivity (ETC) model to predict thermal conductivity of fibrous media as a function of compression. Thermal conductivity of GDL at different operating conditions is essential for accurate thermal modeling in a Proton exchange membrane (PEM) fuel cell stack. Steady state method of guarded hot plate method was used to perform the thermal conductivity measurements and the measurements were carried out on commercially available GDL samples – Toray and SGL (SIGRACET®). GDL thicknesses at different compressions were also measured to calculate the thermal conductivity of GDL at a given compression.

Thermal conductivity of Toray was found to decrease with temperature while that of SGL was constant over temperature. Both Toray and SGL thermal conductivities were observed to increase with compression. Also, contact resistance between GDL-copper surfaces was found to decrease with compression for both Toray and SGL. Furthermore, the effective thermal conductivity model was used to estimate the thermal conductivity of the tested GDL samples at different compressions and was found to match pretty well with the experimentally determined thermal conductivity values.

ACKNOWLEDGEMENT

I am grateful to my advisor Dr. Satish G. Kandlikar for giving me an opportunity to perform some world class research with him. I thank him for the support and guidance to make this work a reality.

I would also like to thank the Department of Mechanical Engineering for opening the door to high quality course work and research. I thank my fellow members of the Thermal Analysis, Microfluidics and Fuel Cell Lab for their help and support.

I would like to appreciate the US Department of Energy for funding this research and also General Motors for providing the necessary technical support and guidance.

Finally, I thank my parents Thiruvanchoor and Lalithambika Radhakrishnan, my brother Anupam, my sister Athira, and my sister-in-law Dimple for their encouragement and support.

TABLE OF CONTENTS

LIST OF FIGURES 7

LIST OF TABLES 10

LIST OF SYMBOLS 11

1. INTRODUCTION 13

    1.1. Proton Exchange Membrane Fuel Cells 15

    1.2. Gas Diffusion Layer 16

2. LITERATURE REVIEW 19

    2.1. Thermal and Water management 19

    2.2. Heat Transfer through Gas Diffusion Layer 21

    2.3. Thermal Conductivity Measurement Techniques for Thin Films 22

        2.3.1. Steady State Method 22

        2.3.2. Transient Method 25

            2.3.2.1. Three ω Method 25

            2.3.2.1. Transient Plane Source (TPS) Method 26

            2.3.2.1. Transient Thermo-Reflectance (TTR) Method 28

    2.4. Previous Work 29

    2.5. Effective Thermal Conductivity (ETC) Models 35

    2.6. Objectives of Present work 38

3. EXPERIMENTAL SETUP AND DATA REDUCTION 40

    3.1. Experimental Setup 40

        3.1.1. Test Section 41

            3.1.1.1. Heater Design 41

3.1.1.2. Cold Plate Design 43
3.1.1.3. Loading system 44
3.1.2. Constant Temperature Bath 45
3.1.3. Power supply 45
3.1.4. Data Acquisition 46
3.2. Experimental procedure and Data Reduction 48
3.2.1. GDL Thickness Measurement 48
3.2.2. Thermal Conductivity Measurement 50
3.2.3. Uncertainty Analysis 53
3.2.3.1. Uncertainty in Heat Applied 54
3.2.3.2. Uncertainty in Thermal Conductivity 54
3.2.3.3. Uncertainty in Unit Area Thermal Resistance 56
3.2.3.4. Uncertainty in Contact Resistance 57
4. RESULTS AND DISCUSSION 59
4.1. GDL Thickness Measurement under Compression 59
4.2. Thermal conductivity Measurement 62
4.2.1. Validation of Test section 62
4.2.2. GDL Thermal Conductivity 62
4.2.3. Effective Thermal Conductivity (ETC) Model 65
4.2.4. Area Thermal Resistance 70
4.2.5. Contact Resistance 72
5. CONCLUSIONS 74
6. REFERENCES 76

7. APPENDIX 79
7.1. Appendix A: Test Section Drawings 79
7.2. Appendix B: MATLAB Codes 82
7.2.1. Effective Thermal Conductivity Model for Toray-060 82
7.2.1. Effective Thermal Conductivity Model for Toray-120 83
7.2.1. Effective Thermal Conductivity Model for SGL-25BC 84
7.2.1. Effective Thermal Conductivity Model for SGL-35BC 85

LIST OF FIGURES

Figure 1: Operating principle of a fuel cell 14

Figure 2: Schematic of a PEM fuel cell 16

Figure 3 (a): SEM image of Carbon cloth (Avcarb) 18

Figure 3 (b): SEM image of Carbon paper (Toray) 18

Figure 4: Schematic for Guarded hot plate method 23

Figure 5: Schematic of test section for steady state method 24

Figure 6: Four pad test structure used in Three ω method 26

Figure 7 (a): Schematic of TPS element 27

Figure 7 (b): Typical TPS element temperature rise during transient measurement 27

Figure 8: Schematic of Transient Thermo Reflectance (TTR) system 29

Figure 9: Schematic of test section used by Vie et al. for in-situ thermal conductivity measurement of GDL 30

Figure 10: Schematic of test section used by Khandelwal et al. for steady state thermal conductivity measurement of GDL 32

Figure 11: Schematic of test section used by Nitta et al. for steady state thermal conductivity measurement of GDL 34

Figure 12 (a): Schematic of Parallel model 36

Figure 12 (b): Schematic of Series model 36

Figure 12 (c): Schematic of Krischer model 36

Figure 12 (d): Schematic of Maxwell Eucken model 36

Figure 12 (e): Schematic of Effective Medium theory model 36

Figure 13: Plot of effective thermal conductivity of GDL for different models 38

Figure 14: Schematic of experimental setup 41

Figure 15 (a): Pro-E drawing of Main heater design 42

Figure 15(b): Pro-E drawing of Guard heater design 42

Figure 15 (c): Pro-E drawing of Heater assembly 42

Figure 16: Pro-E drawing of cold plate 44

Figure 17: Front panel view of LabVIEW used for data acquisition 46

Figure 18: Test section used for GDL thickness measurement 48

Figure 19 (a): Principle of GDL thickness measurement 50

Figure 19 (b): Principle of compressed GDL thickness measurement 50

Figure 20: Test section used for thermal conductivity measurement 51

Figure 21: Plot of GDL thickness versus compression for Toray-060, Toray-120, SGL-25BC and SGL-35BC GDL samples 60

Figure 22: Schematic of thickness versus compression plot to calculate GDL thickness at zero load 60

Figure 23: Plot of Thermal conductivity versus Temperature for Toray and SGL GDL samples at 0.04 MPa compression 63

Figure 24: Thermal conductivity plot as a function of compression for Toray and SGL GDL samples at 58°C 64

Figure 25: Comparison of experimental thermal conductivity with that predicted by the model for Toray-060 67

Figure 26: Comparison of experimental thermal conductivity with that predicted by the model for Toray-120 67

Figure 27: Comparison of experimentally thermal conductivity with that predicted by the model for SGL-25BC 68

Figure 28: Comparison of experimental thermal conductivity with that predicted by the model for SGL-35BC 68

Figure 29: Area thermal resistance versus compression for Toray-060 and Toray-120 70

Figure 30: Area thermal resistance versus compression for SGL-25BC and SGL-35BC 71

Figure 31: Plot of contact resistance of GDL-copper pair versus compression for Toray and SGL GDL samples 72

LIST OF TABLES

Table 1: Thermal conductivity values of fuel cell components reported by Khandelwal et al.....33

Table 2: Thermal conductivity of GDL at 20ºC reported by Ramousse et al. 33

Table 3: Dimensions of Main Heater, Guard Heater and Cold Plate 43

Table 4: Load cell calibration data provided by manufacturer 45

Table 5: GDL thickness at zero load 61

Table 6: Comparison of Thermal Conductivity of PTFE sheet with published values 62

LIST OF SYMBOLS

English

T	Temperature (K)
Q	Heat transfer rate (W)
k	Thermal conductivity (W/m-K)
A	Heat transfer area (m^2)
L	Thickness (m)
P	Power (W)
V	Voltage (V)
I	Current (A)
R	Resistance (K/W)
R''	Area thermal resistance (m^2-K/W)
CR	Compression ratio

Greek

ϵ	Volume fraction
Δ	Difference

Subscript

f	Fluid
C	Carbon fiber
ser	Series Model
par	Parallel Model
eff	Effective
CR	Contact Resistance
Total	Total
th	Thermal
1	Thickness 1
2	Thickness 2
0	Zero load thickness
c	Compressed
actual	Actual
apparent	Apparent

1. INTRODUCTION

Fuel cell is an electrochemical energy conversion device which converts chemical energy in the fuel directly into electric energy. The fuel (at the anode side) and the oxidant (at the cathode side) react in the presence of an electrolyte to produce electricity, water and heat. Fuel cell is similar to a battery except for the fact that fuel cells can be operated continuously as long as it is provided with the required amount of fuel and oxidant. With the depletion of fossil fuels and growing concerns over environmental issues such as global warming, there has been a keen interest in research related to fuel cells. High efficiency, silent operation and zero pollution make fuel cell a strong candidate as an alternate energy conversion device to traditional internal combustion engines.

Figure 1 depicts the general operating principle of a Proton Exchange Membrane (PEM) fuel cell. Electrons are released as a result of oxidation of fuel at the anode while protons are transferred through a layer of electrolyte to the cathode where they combine with electrons and oxygen to form water. There are six major types of fuel cells. They are:

1. Proton exchange membrane fuel cell
2. Direct methanol fuel cell
3. Phosphoric acid fuel cell
4. Alkaline fuel cell
5. Molten carbonate fuel cell
6. Solid-oxide fuel cell

Although the basic principle of these fuel cells is the same, their operating characteristics like temperature range, type of materials used and performance characteristics may vary.

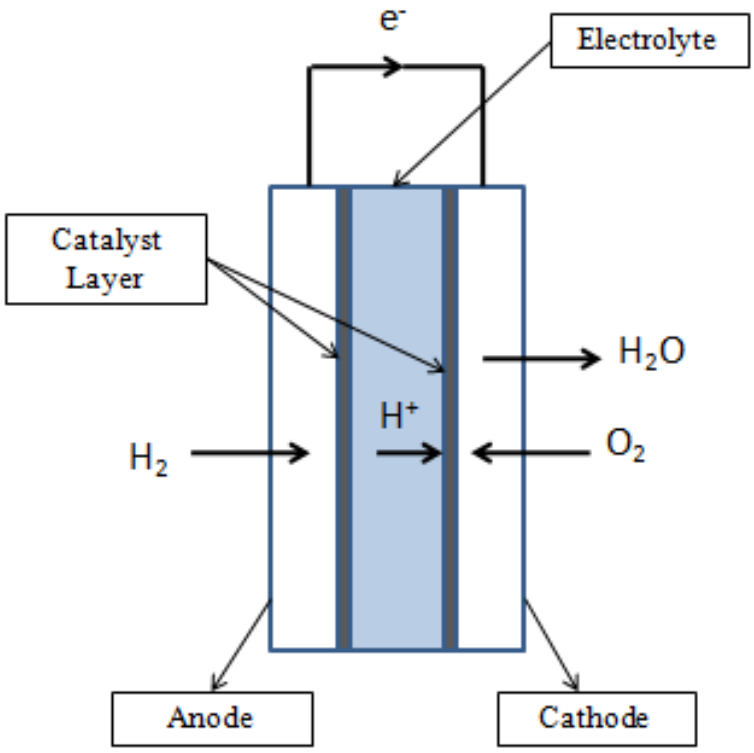

Figure 1: Operating principle of a fuel cell.

Fuel cell combines the advantages of both combustion engine as well as a battery. The use of hydrogen as fuel will greatly reduce the polluting CO and NO_x emissions. In addition, fuel cells have no moving parts, resulting in a higher operating efficiency, silent operation and lower maintenance. However, there are some disadvantages which have inhibited the implementation of fuel cell technology namely, high cost, lower power densities, thermal and water management issues, fuel handling, and storage problems.

The common applications of fuel cells include portable, stationary and transportation applications. Each application may require a particular type of fuel cell. Portable applications require compact and high power density systems whereas stationary applications are designed for

continuous operation thereby requiring durable and highly efficient systems. Rapid start-up, high energy density, compact size, and high efficiency are some of the desired features for fuel cells for transportation applications. Some of the other important applications of fuel cells include combined heat and power systems, military communication equipments.

1.1. Proton Exchange Membrane Fuel Cells

Proton exchange membrane (PEM) fuel cells are most attractive for transportation application because of their low operating temperature, high power density and fast start-up capability. In PEM fuel cells, hydrogen is used as the fuel and a thin polymer membrane acts as the electrolyte. A typical PEM fuel cell stack (see Fig. 2) consists of Membrane Electrode Assembly (MEA) which includes the membrane, anode and cathode catalyst layers; Gas Diffusion Layer (GDL); and Bipolar plates with flow channels for reactants. Hydrogen fuel and oxygen from air are channeled to the anode and cathode sides of the fuel cell, respectively, through flow channels (Bipolar plates). At the anode, the reaction with platinum catalyst causes hydrogen to split into protons and electrons. The membrane permits only protons to pass through to the cathode while the electrons are forced through an electric circuit. Finally, at the cathode, protons and electrons combine with oxygen to produce water, which must be removed. The half cell reactions and overall reaction are as follows:

Anode reaction: $$H_2 -> 2H^+ + 2e^- \quad (1)$$

Cathode reaction: $$\frac{1}{2}O_2 + 2e^- + 2H^+ -> H_2O \quad (2)$$

Overall reaction: $$H_2 + \frac{1}{2}O_2 -> H_2O \quad (3)$$

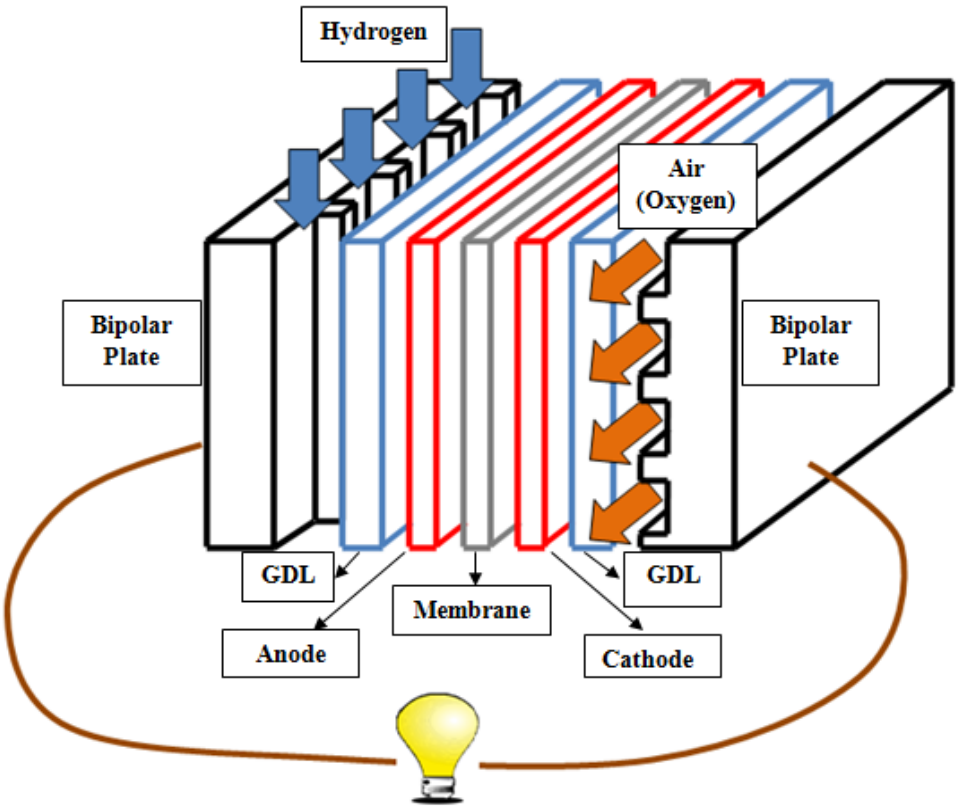

Figure 2: Schematic of a PEM fuel cell.

1.2. Gas Diffusion Layer

Gas diffusion layer (GDL) is one of the critical components in a PEM fuel cell stack. In the stack, GDL is placed between the catalyst layer and the bipolar plates on both anode as well as cathode sides. It has a heterogeneous, fibrous structure with fibers having diameters in the order of 10µm. The thickness of GDL is usually, in the range of 200-400µm.

The most important function of GDL is to uniformly distribute reactant gases from the flow channels to the catalyst layer and to remove product water from the catalyst layer area to the

flow channels. GDL also provides the necessary electrical conductivity between the catalyst layer and bipolar plates where the current collectors are located. Furthermore, it aids in removing the waste heat produced inside the fuel cell to the cooling channels which are also located on the bipolar plates. Finally, it provides mechanical support to the fuel cell stack and maintains good electrical and thermal contact with the catalyst layer. GDLs are generally made hydrophobic in order to avoid flooding which may cause the fuel cell to accumulate water and block gas flow pathways to the reaction sites. Carbon fiber based products are usually used as GDL because of their good electrical conductivity and high porosity (>70%) [1] and are made of two types:

1. Non-woven carbon paper;
2. Woven carbon cloth.

Figure 3 shows SEM images of carbon paper and carbon cloth. Carbon paper has a webbed structure bounded together by carbonized thermosetting resins which make the paper fairly brittle. Carbon cloth has a woven structure which provides the necessary mechanical integrity. Carbon cloth is generally thicker than paper. Mathias et al. [1] have found carbon cloth to be more compressible than carbon paper.

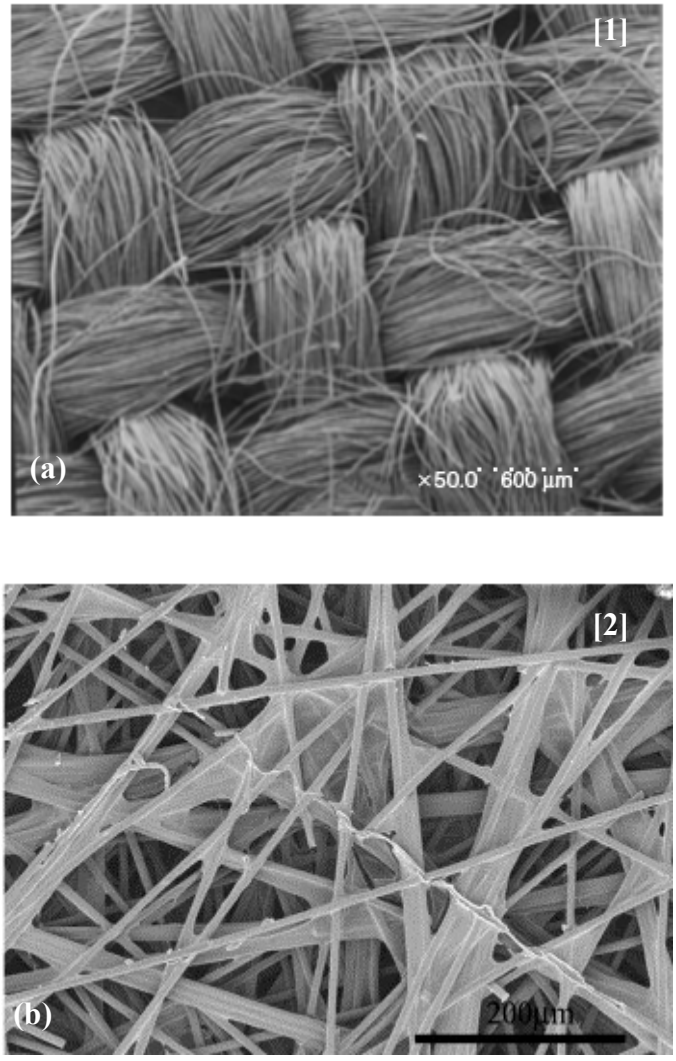

Figure 3: SEM image of (a) Carbon cloth (Avcarb), (b) Carbon paper (Toray).

2. LITERATURE REVIEW

An extensive literature review is done to investigate the need to measure the thermal conductivity of GDL. Furthermore, the different measurement techniques used for thermal conductivity measurement of thin films are reviewed to select the most suitable method for the case of GDL. Also, the previous works done in thermal conductivity measurement of GDL are reviewed for better understanding of the different methodologies used and the trend of results obtained. Different effective thermal conductivity models are also reviewed in this chapter to develop a mathematical model to predict the thermal conductivity of GDL as a function of compression.

2.1. Thermal and Water Management

Operating temperature of a fuel cell is critical for its optimum performance. Theoretically, increase in operating temperature will cause a drop in maximum theoretical voltage, thereby causing a reduction in the theoretical efficiency. This can be explained by using the Nernst equation:

$$E = E_o - \frac{RT}{nF} ln\left(\frac{a_{product}}{a_{reactants}}\right) \quad (4)$$

where, E_0 is the open circuit voltage, E is theoretical cell voltage, R is the characteristic gas constant, T is the temperature, n is the number of moles, F is the Faradays constant, $a_{products}$ is the activity of products and $a_{reactants}$ is the activity of reactants.

However, a higher operating temperature at the electrodes increases the electrochemical activity of the cell which in turn improves the efficiency. It can be noted that there is a moderate temperature range for each type of fuel cell (80-90ºC for PEM fuel cells) within which it

operates effectively. Hence, the purpose of thermal management is to ensure that the fuel cell operation is within this specific temperature range. PEM fuel cells are usually 50% efficient, which implies that the remaining 50% is the waste heat that needs to be removed [3]. Optimal thermal management should therefore also account for the effective use of waste heat from fuel cell as to increase the overall system efficiency.

Yu et al. [4] used the maximum temperature in the fuel cell as the operating temperature to develop a thermal management strategy for fuel cells with large active area. They concluded that the maximum temperature must be monitored and controlled for durability and proper thermal management of the cell.

Water management is another critical issue for optimum performance and longevity of PEM fuel cells. The membrane of PEM fuel cell must maintain at least a minimum hydration level for it to conduct protons. Insufficient amount of water in the fuel cell would lead to a higher membrane resistance and membrane dry out, resulting in premature failure of the fuel cell. At the same time, excess water in the fuel cell would cause an increase in the mass transport loss at the cathode side resulting in cell degradation. Hence, the desired objective of a water management scheme is to maintain a correct water balance in the fuel cell.

Thermal and water management include heat and water utilization, cooling and humidification processes. A detailed knowledge of the temperature distribution within the fuel cell is essential for proper thermal and water management of PEM fuel cell. The local temperature variation within a fuel cell is mainly due to the heat generated as a result of electrochemical reaction, and also due to the joule heating in all the components, especially at the electrolyte. This temperature distribution can cause flooding or drying of the cell which may

result in cell degradation. Hence, a thorough understanding of temperature distribution within the cell is essential for proper thermal and water management. Due to the difficulty in direct temperature measurement within the fuel cell, various models have been used to estimate the temperature distribution. However, this estimation is not accurate unless the thermal conductivities of different components in the fuel cell at different operating conditions are known.

2.2. Heat Transfer through Gas Diffusion Layer

Heat transfer through a GDL is complex because of the existence of both solid and fluid phases, and also due to the random pore morphology. The mode of heat transfer varies for different pore structures. It is well known that conduction, convection and radiation are the three modes of heat transfer. In a porous media, heat transfer due to convection occurs when there is a flow within the pores [5]. The effect of convective heat transfer is more apparent in the case of large pore sizes, but can be neglected for small pores (<100μm) at lower temperatures because of the lack of intense fluid circulation in the pores [6].

Radiation heat transfer occurs through heat emission of pore walls. Heat transfer due to radiation is significant for pores of sizes greater than 10μm, if the pore temperature is above 1000K [6]. Hence in GDL, radiation heat transfer can be neglected as the operating temperature of PEM fuel cell is generally below 373K. In short, it can be concluded that conduction is the predominant mode of heat transfer in a GDL.

2.3. Thermal Conductivity Measurement Techniques for Thin Films

Thermal conductivity is the measure of a material's ability to transmit heat. It is the proportionality factor in Fourier's Law for heat conduction equation.

$$Q = -kA\frac{dT}{dx} \tag{5}$$

where, Q is the heat transfer rate, A is the heating area, k is the thermal conductivity, dT/dx is the temperature gradient.

The values of thermal conductivity vary with temperature, compression, chemical composition, physical structure, state of substance. Moisture content also affects the thermal conductivity of a material. Generally there are two techniques for the measurement of thermal conductivity of any material. They are:

1. Steady state method
2. Transient method

Thermal conductivity is an important material parameter in the heat transfer through inhomogeneous porous GDL. These two above mentioned techniques may also be applied to determine the thermal conductivity of GDL.

2.3.1. Steady State Method

Guarded Hot Plate Method [7] is the most widely used method to determine the thermal conductivity of low thermal conductivity materials in which the heat flow is steady and unidirectional. In this method, two identical test samples are placed on either sides of a flat heater comprising of main heater and annular guard heater (see Fig. 4). The heater sample

stack is then sandwiched between two heat sinks which are liquid cooled to maintain at a fixed temperature.

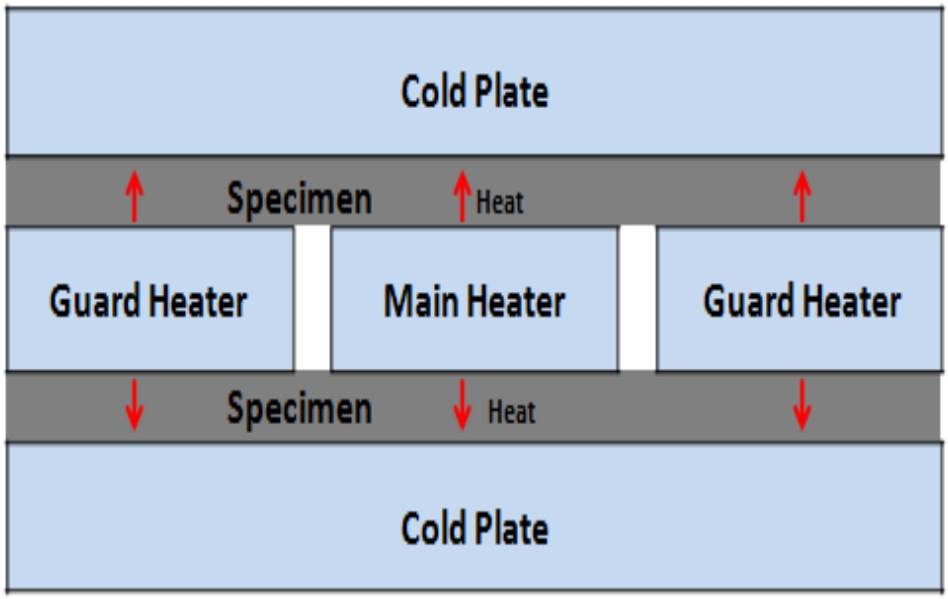

Figure 4: Schematic for Guarded hot plate method.

The guard heater provided around the main heater is maintained at the same temperature as that of the main heater to prevent any radial heat loss. At steady state condition, the heat input to the heater is assumed to be all transferred across the sample and thermal conductivity of the sample is calculated using Fourier equation as:

$$k = \frac{Q\,L}{2A\,\Delta T} \tag{6}$$

The factor 2 in the denominator is provided as the heat flux is assumed to be equally divided between the two samples.

Another steady state method [12] used to measure the thermal conductivity of thin films (see Fig. 5) consists of the test sample sandwiched between two standard materials of known thermal conductivity. The standard materials are in turn compressed by two backing plates (hot and cold plates) which act as heat source and sink, respectively. The hot and cold plates together apply a uniform heat flux through the sample. By measuring the temperature drop across the sample, thermal conductivity can be calculated as:

$$Q = k\,A\,\frac{\Delta T}{L} \tag{7}$$

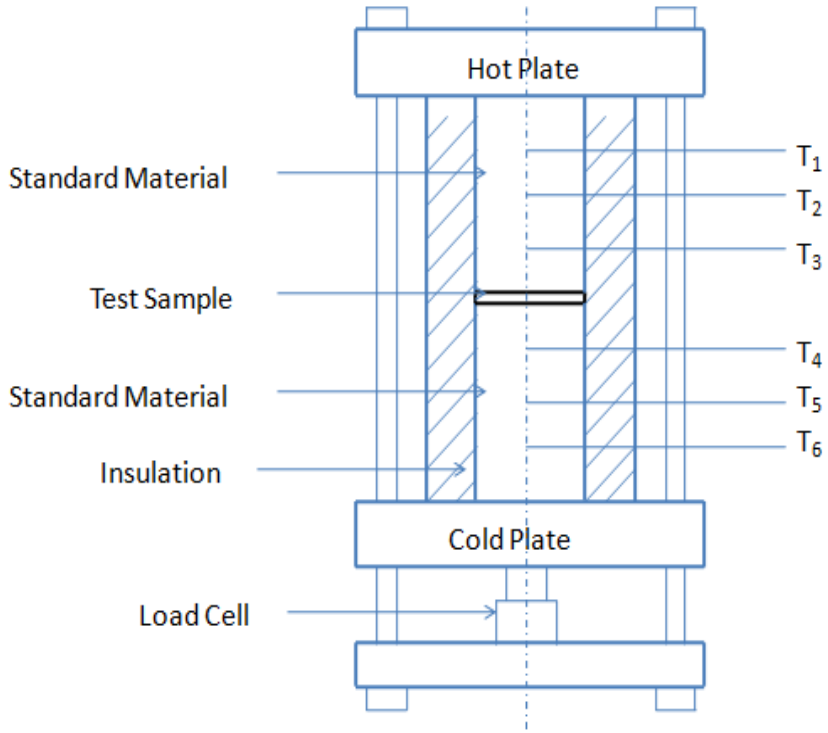

Figure 5: Schematic of test section for steady state method.

2.3.2. Transient Method

The procedure for determining the thermal conductivity in transient method is to apply a steady heat flux across the sample and to measure the temperature rise at a point in the sample after a certain period of time. This technique uses either a line heat source or a plane heat source. The different transient methods that can be used for thin films are discussed below.

2.3.2.1. Three ω Method

This method uses a line heat source for heating the sample. A thin electrical wire is deposited on the sample which acts as the heater as well as the temperature sensor [8]. Figure 6 shows the four pad test structure used for thermal conductivity measurement in which current at a frequency of ω is supplied producing joule heating in the sample at a frequency of 2ω. The 3ω component of voltage drop across the metal line is proportional to the temperature drop which is used to determine the sample thermal conductivity.

$$V_{3\omega} = \frac{I_0 R_0 \alpha_T \Delta T}{2} \tag{8}$$

$$k = \frac{P L}{2b \Delta T} \tag{9}$$

where, $V_{3\omega}$ is 3ω component of output voltage, I_0 is the input current along the strip, R_0 is the resistance between inner pads, α_T is the temperature coefficient of resistivity, b is half length of metal line, P is the power supplied and L is the thickness of the sample.

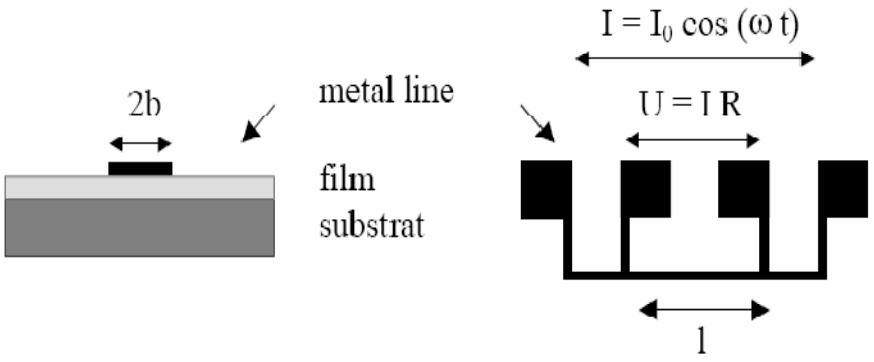

Figure 6: Four pad test structure used in Three ω method.

2.3.2.2. Transient Plane Source (TPS) Method

This method uses a plane source for heating in which the transient plane source (TPS) element behaves both as a heater as well as a temperature sensor. The TPS element consists of nickel double spiral sandwiched between two electrically insulating sheets (kapton or mica). A constant electric power is supplied to the TPS element which is in contact with two samples of the same material on either side, and the increase in temperature (ΔT) is calculated as:

$$\Delta T\ (t) = \frac{1}{\alpha}\left(\frac{R(t)}{R_0} - 1\right) \tag{10}$$

where, R_0 and $R(t)$ are the initial resistance and resistance at time t of the TPS element and α is the coefficient of thermal expansion. Typical temperature variation during TPS measurement is as shown in Fig. 7(b). The average increase in temperature can be theoretically derived as:

$$\Delta T = P\ (\pi^{1.5}\alpha k)^{-1} D(t) \tag{11}$$

where, P is the power output, a is the sensor radius and $D(t)$ is a geometric function. Thermal conductivity can be obtained by fitting the experimental temperature rise (Eqn. (10)) to the straight line data given by Eqn. (11).

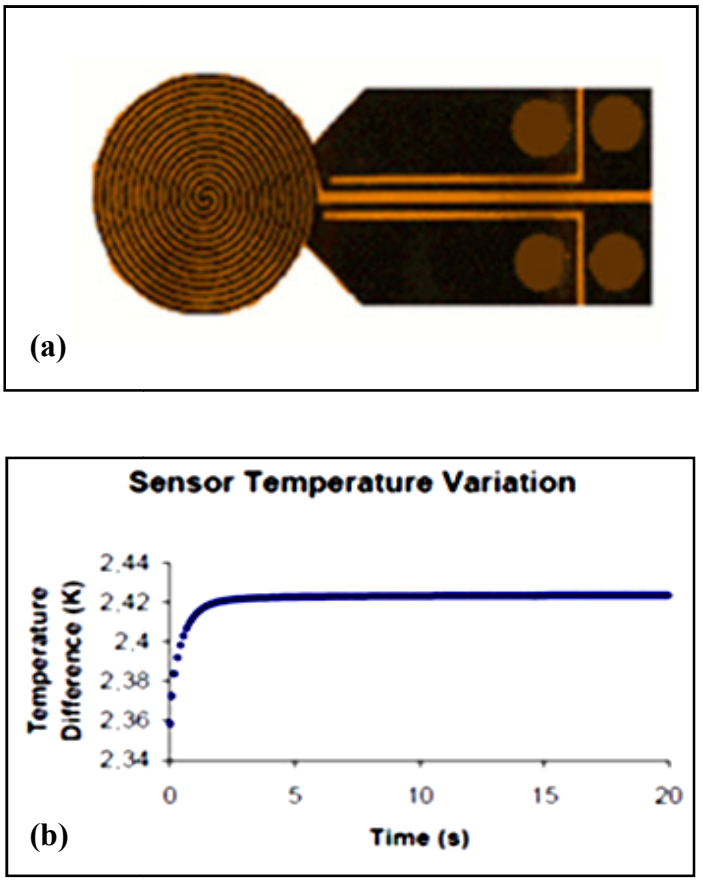

Figure 7: (a) Schematic of TPS element, (b) Typical TPS element temperature rise during transient measurement.

2.3.2.3. Transient Thermo-Reflectance (TTR) Method

Transient thermo-reflectance (TTR) method is a non-contact and non-destructive method used to determine the thermal properties of thin films used in microelectronic devices. The principle used here is to heat the sample to a particular temperature by using laser irradiation and to record the changes in the surface reflectivity of the sample. The sample is generally heated using pulsed laser with short pulse duration. The depth of heating depends on the laser pulse wavelength as well as the surface properties. After each pulse, the sample is allowed to cool down to the ambient temperature during which the probe laser reflected from the sample gives the instantaneous surface reflectivity. These changes in surface reflectivity are linearly proportional to the changes in surface temperature [10] which are recorded using an oscilloscope. The thermal conductivity of the sample is then extracted from the recorded temperature response by fitting a numerical transient temperature response for the same physical problem. The schematic for TTR system is shown in Fig. 8.

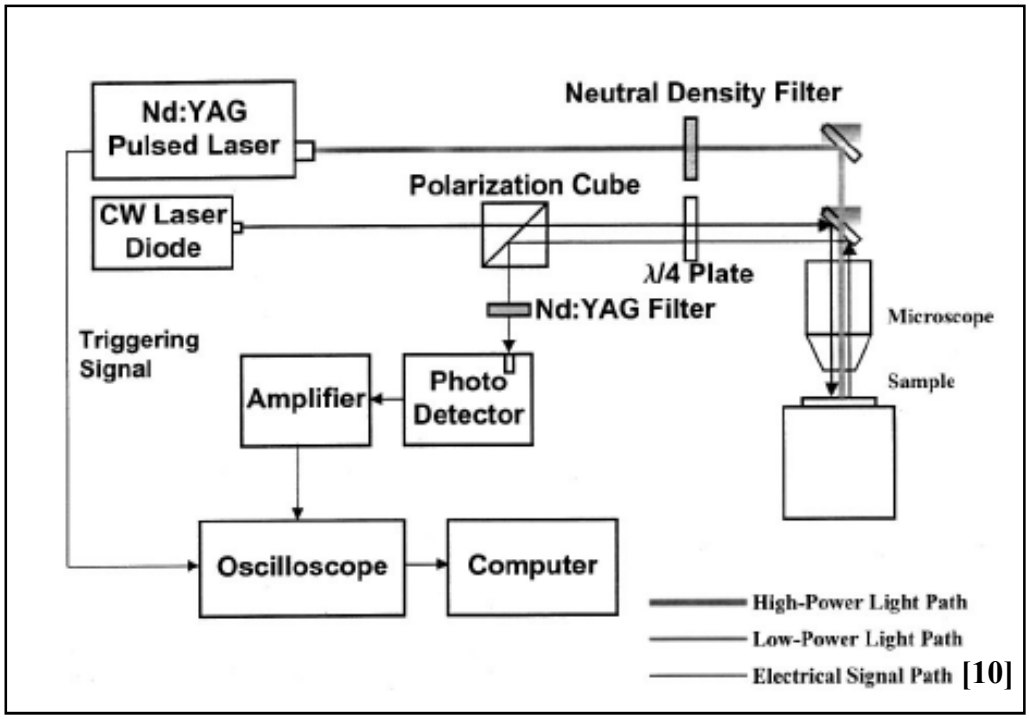

Figure 8: Schematic of Transient Thermo Reflectance (TTR) system.

2.4. Previous Work

One of the first attempts to estimate the thermal conductivity of different components in a fuel cell stack was carried out by Vie et al. [11] in 2003. Their study determined the thermal conductivity of fuel cell membrane and GDL by measuring the temperature at different locations in the fuel cell stack. In the experimental setup thermocouples were inserted at different locations to measure the temperature gradients as shown in Fig. 9.

A membrane of area 5 cm^2 with a Nafion content of 35% was used for the testing and the GDL used was ETEK ELAT with a platinum loading of 0.1 mg/cm^2. The thermocouples used were K-type with diameters ranging from 36-120 μm and were sandwiched between the different components in the stack. The stack was mechanically compressed to a pressure of 10 bar.

Hydrogen and oxygen gases were humidified at 80ºC with gas pressures at 4.5 bar. The temperatures were recorded when the system reached steady state for different current densities. They found that the average thermal conductivity of GDL and catalyst layer to be 0.2±0.1 W/m-K. Also, the study estimated negative values for thermal conductivities of dry membrane. These unphysical values were due to thickness of the thermocouples embedded into the stack causing uneven compression, and also due to the blocking of some of the active area by the thermocouples.

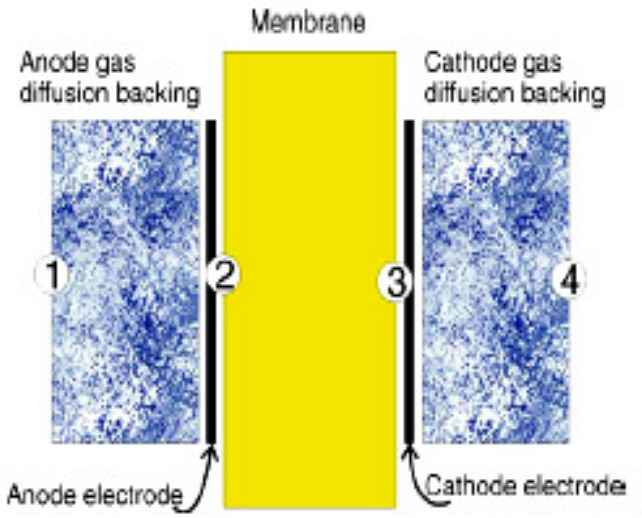

Figure 9: Schematic of test section used by Vie et al. for in-situ thermal conductivity measurement of GDL.

A more accurate method to measure the thermal conductivity of fuel cell components was developed by Khandelwal et al. [12] in 2006. They performed experiments to measure the thermal conductivity of dry Nafion, GDL and catalyst layer as a function of different conditions like compression, PTFE content, etc. They also measured the thermal contact resistance between GDL and Aluminum plate. The method used for the thermal conductivity measurement was 1-D steady state method. The test section, (see Fig. 10), had the sample sandwiched between two standard materials of known thermal conductivity. The standard material used was aluminum bronze with the thermocouples inserted at different locations to measure the heat flux applied. A hot plate and a cold plate were placed on top and bottom respectively, making contact with the standard material to produce a temperature gradient through the sample. The experiments were carried out for two different thicknesses of the sample to eliminate the thermal contact resistance error from the thermal conductivity value determined which is given by the equation:

$$k = \frac{L_1 - L_2}{A\,(R_{Total\,1} - R_{Total\,2})} \tag{12}$$

Table 1 shows the thermal conductivity values determined for Nafion membrane, different GDLs - Toray, SIGRACET and ETEK ELAT.

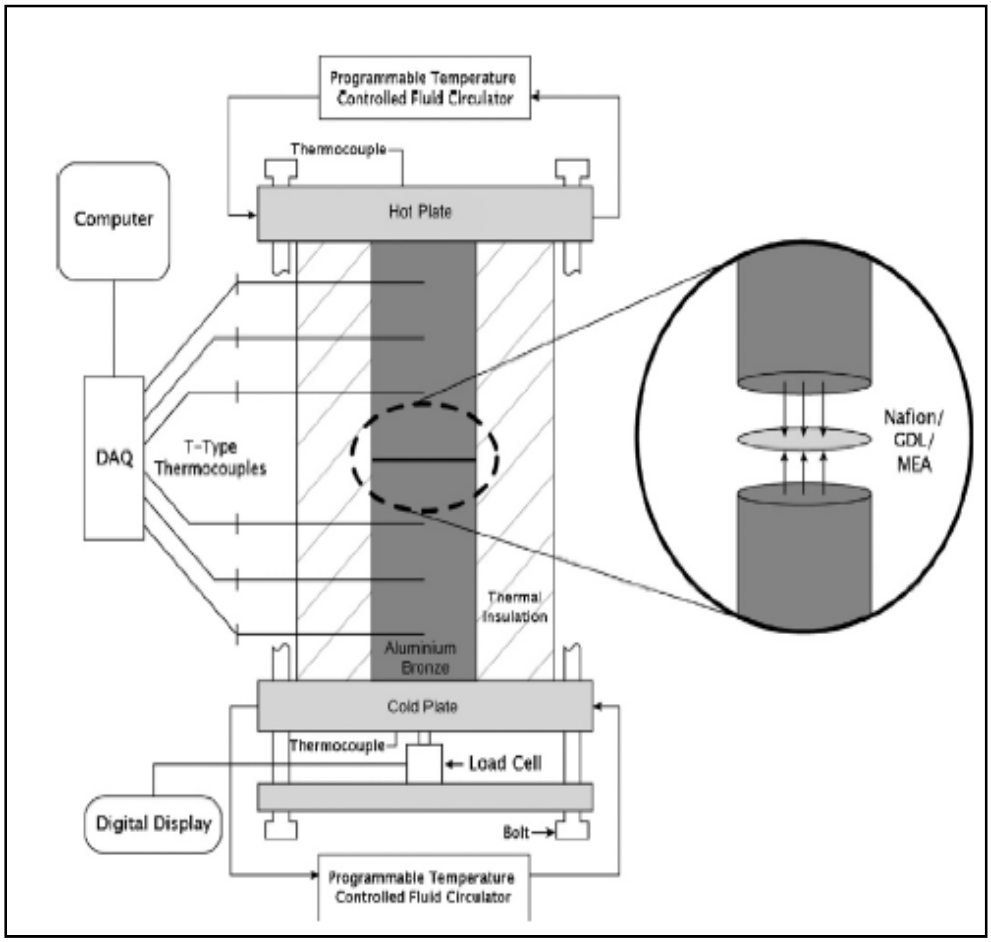

Figure 10: Schematic of test section used by Khandelwal et al. for steady state thermal conductivity measurement of GDL.

Table 1: Thermal conductivity values of fuel cell components reported by Khandelwal et al.

Sample	Measured Thermal conductivity (W/m-K)
Toray GDL (~26°C)	1.80±0.27
SIGRACET 0 wt % PTFE (56°C)	0.48±0.09
SIGRACET 5wt % PTFE (58°C)	0.31±0.06
SIGRACET 20 wt % PTFE (58°C)	0.22±0.04
E-Tek ELAT (33°C)	0.22±0.04

The same method developed by Khandelwal et al. [12] was used by Ramousse et al. [5] in 2007 to determine the thermal conductivity of carbon felts used as GDL in PEM fuel cells. The standard material used for the study was copper and the tests were conducted for two different thicknesses of the sample in vacuum by placing the test section inside a bell jar. The thermal conductivity values obtained for different GDL samples are shown in Table 2.

Table 2: Thermal conductivity of GDL at 20ºC reported by Ramousse et al.

Sample	Thickness (µm)	k_{min} (W/m-K)	k_{max} (W/m-K)
Quintech	190	0.36	1.36
Quintech	280	0.33	0.59
Quintech	230	0.20	0.30
SGL Carbon	420	0.26	0.34

Nitta et al. in 2008 [13] evaluated the mechanical and thermal properties of GDL as a function of compression. The study also provided the thermal contact resistance between GDL and Graphite surfaces. The methodology used for the measurement was a steady state method with the GDL sample sandwiched between two graphite rods (see Fig. 11). The GDL sample used for testing was SGL 10 BA. Temperature probes located at four points (see Fig. 11) in the test section were used to measure the steady state temperatures. The equation used to calculate the thermal conductivity is as follows:

$$k_{GDL}(h) = \frac{h}{R_{b,GDL}(h)} = \frac{h}{s} Q_{GDL} \tag{13}$$

where, $R_{b,GDL}$ is the thermal resistance of GDL, k_{GDL} is the thermal conductivity of GDL, Q_{GDL} is the heat transfer rate through the GDL, h is the GDL thickness, and S is the cross-sectional area. Thermal conductivity of the GDL sample (SGL 10 BA) was found to be 1.8 ± 0.11 W/m-K, and also to be independent of compression. Furthermore, thermal contact resistance between GDL sample and graphite was found to decrease nonlinearly with compression.

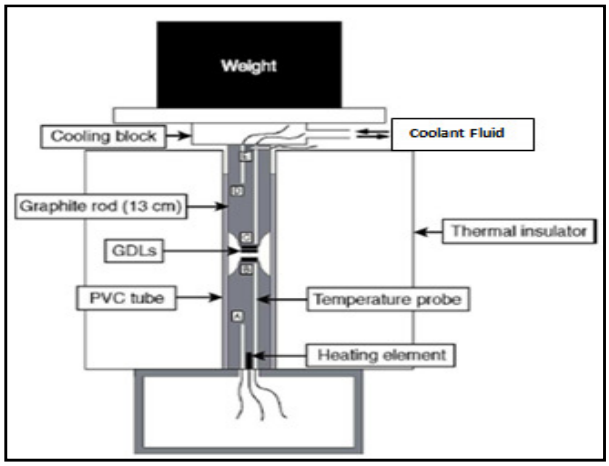

Figure 11: Schematic of test section used by Nitta et al. for steady state thermal conductivity measurement of GDL.

2.5. Effective Thermal Conductivity (ETC) Models

It is known that GDL used in PEM fuel is a heterogeneous material with a fibrous structure, and also the heat transfer through the GDL is dominated by conduction. Many models have been described in literature ([14], [15], [16], [17], [18]) to estimate the effective thermal conductivity of heterogeneous materials. The fundamental models (see Fig. 12) used for the estimation of effective thermal conductivity are as follows:

1. Parallel model;
2. Series model;
3. Krischer (series-parallel) model;
4. Maxwell Eucken (M-E) model;
5. Effective Medium Theory (EMT) model;
6. Co-continuous model.

Parallel model [19] considers the thermal resistances to be parallel to the heat flow. It represents the upper bound of effective thermal conductivity of any heterogeneous material. The effective thermal conductivity of a composite material with two components using parallel model is as follows:

$$k_{eff} = \epsilon_f k_f + \epsilon_C k_C \tag{14}$$

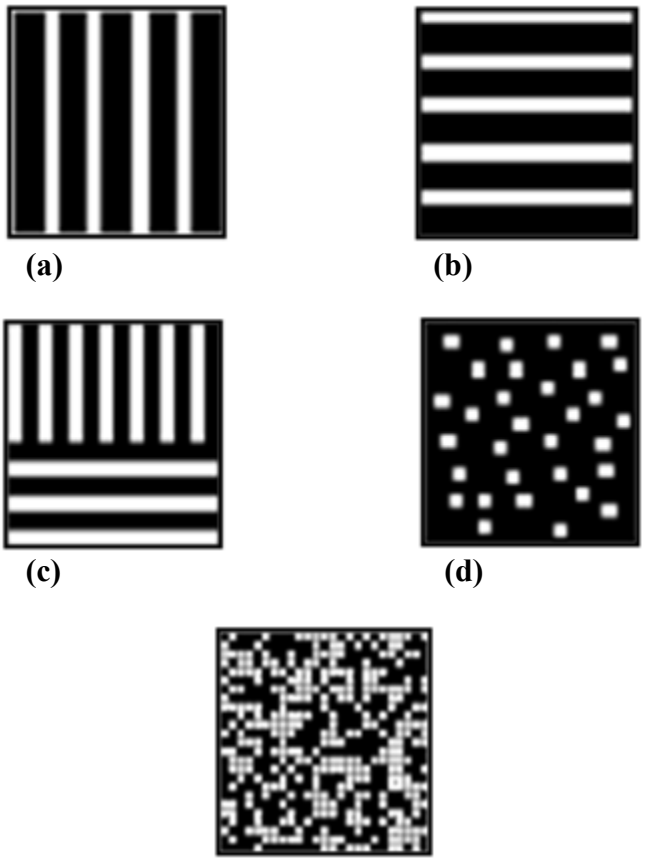

Figure 12: Schematic of a.) Parallel model, b.) Series model, c.) Krischer model, d.) Maxwell Eucken model, e.) Effective Medium theory model.

Series model [19] considers the thermal resistances to be series and predicts the lower bound of effective thermal conductivity. The equation for effective thermal conductivity using series model is given by:

$$k_{eff} = \frac{1}{\frac{\epsilon_f}{k_f}+\frac{\epsilon_C}{k_C}} \tag{15}$$

Since, series and parallel models define the lower and upper bound of effective thermal conductivity of any heterogeneous material any structure could be modeled as a combination of series and parallel structures, which is the Krischer model [14]. The effective thermal

conductivity from this model is given by Eqn. (16). Here, f is the weighting parameter or distribution factor.

$$k_{eff} = \frac{1}{\frac{f}{k_{ser}}+\frac{1-f}{k_{par}}} \left.\begin{array}{l} \\ \\ \end{array}\right\} \begin{array}{l} f = 0, Parallel \\ f = 1, Series \end{array} \tag{16}$$

Maxwell Eucken (M-E) [14] model assumes the heterogeneous material to be composed of a dispersion of small spheres in a continuous matrix of another component. Here, the spheres are considered to be far apart such that local variations in the temperature distribution of sphere do not influence the neighboring spheres. With this concept, two M-E equations have been developed – one with air as the continuous medium, and the other with carbon fiber as the continuous medium and are as follows:

$$k_{eff} = k_f \frac{2k_f+k_C-2(k_f-k_C)\epsilon_C}{2k_f+k_C+2(k_f-k_C)\epsilon_C} \tag{17}$$

$$k_{eff} = k_C \frac{2k_C+k_f-2(k_C-k_f)\epsilon_f}{2k_C+k_f+2(k_C-k_f)\epsilon_f} \tag{18}$$

In Effective Medium Theory (EMT) model [14], the components are considered to be randomly distributed in the material with neither phase being necessarily continuous or dispersed. The effective thermal conductivity for this model is given by Eqn. (19):

$$\epsilon_f \frac{k_f-k_{eff}}{k_f+2k_{eff}} + \epsilon_C \frac{k_C-k_{eff}}{k_C+2k_{eff}} = 0 \tag{19}$$

Co-continuous model [18] assumes that all phases/components are mutually continuous. The effective thermal conductivity for a co-continuous model is derived by considering a dispersed phase to be split between two continuous phases. Although, co-continuous model is independent

of series and parallel models, the equation for the effective thermal conductivity for co-continuous model can be expressed as a function of parallel and series effective thermal conductivities.

$$k_{eff} = \frac{k_{ser}}{2}\left(\sqrt{1 + 8\frac{k_{par}}{k_{ser}}} - 1\right) \tag{20}$$

Figure 13 shows the effective thermal conductivity of heterogeneous porous material with carbon fiber and air as the two components predicted using the above discussed models.

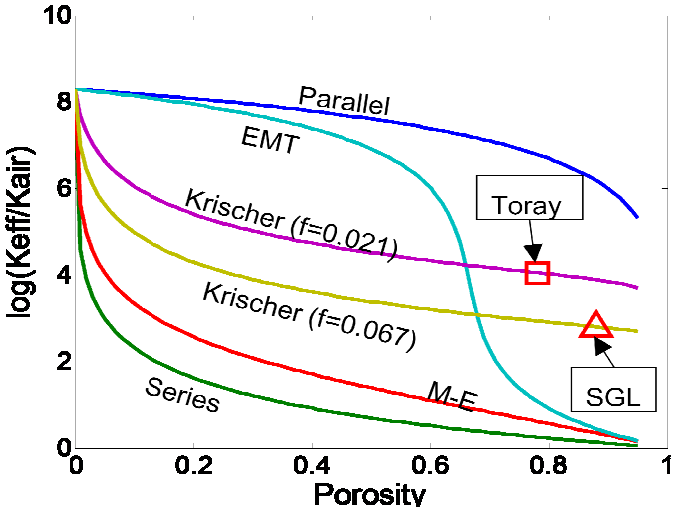

Figure 13: Plot of effective thermal conductivity of GDL for different models.

It can be inferred from the plot that parallel and series models predict upper and lower bound of effective thermal conductivity, respectively. Also, Krischer model can be used to predict the thermal conductivity of both Toray and SGL GDL.

2.6. Objectives of Present Work

After an extensive literature review, it became clear that thermal and water management are closely related to each other and are essential for achieving the optimum performance, durability

and longevity of PEM fuel cell. Temperature distribution within the cell may cause local hot spots in case of improper thermal and water management. Hence, thermal modeling is required for achieving optimum performance and for the thermal management of fuel cells. In order to perform thermal modeling of the fuel cell, a good knowledge of thermal conductivities of different components like gas diffusion layer, membrane, etc. in a fuel cell stack are critical. The literature review on previous research on GDL thermal conductivity ascertains that the thermal conductivity is not the same for all GDLs. The present study will develop a method to experimentally determine the thermal conductivity of GDL as a function of temperature and compression for different commercially available GDL samples. The work also will measure the thermal contact resistance between the GDL and copper surface.

3. EXPERIMENTAL SETUP AND DATA REDUCTION

The guarded hot plate method was chosen from the different thermal conductivity measurement techniques explained in the literature review to measure thermal conductivity of GDL because of its minimal radial heat loss, simple design and low cost. This chapter describes in detail the experimental setup used, the procedures to measure thickness and thermal conductivity of GDL, and also analyzes the uncertainty involved in the experimental results.

3.1. Experimental Setup

The experimental system described in this section is used to measure thermal conductivity of GDL as a function of temperature and compression. The schematic of the entire system is shown in Fig. 14. The system consists of several subsystems which include the test section, constant temperature bath, loading clamp and load cell, power supply and data acquisition system. Detailed description of each sub-system is presented in the following sections.

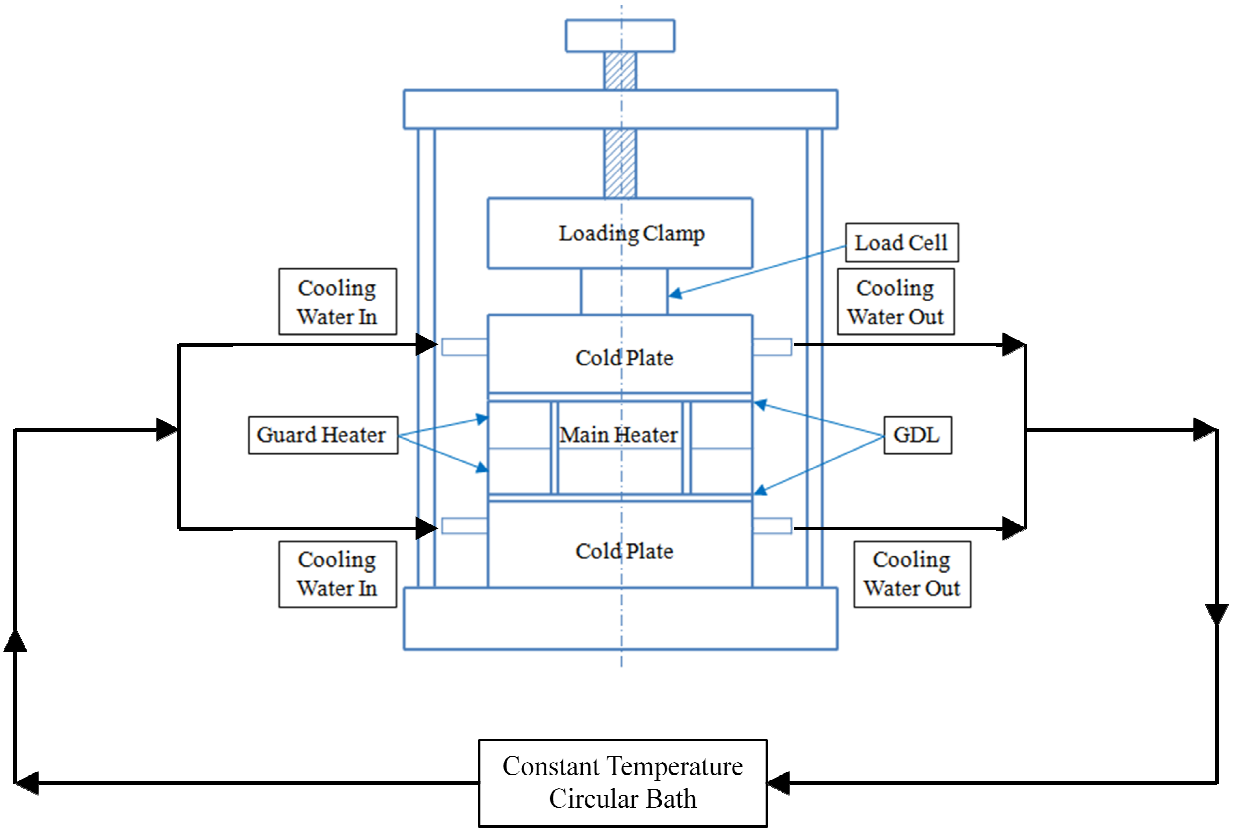

Figure 14: Schematic of experimental setup.

3.1.1. Test Section

The test section consists of the heaters (main and guard heaters), cold plates which act as the heat sinks, loading clamp to apply compression, and load cell to measure the compressive force applied.

3.1.1.1. Heater Design

The heater used consists of two main parts:

1. Main heater
2. Guard heater

The main heater is used to apply a constant heat flux through sample while the annular guard heater is maintained at the same temperature as that of the main heater so that the entire heat is transferred through the sample thereby minimizing radial heat losses. The heater material used is copper due to its high thermal conductivity aiding in achieving a constant plate temperature. Both the heaters are designed to be cylindrical with dimensions as shown in Table 3. Three concentric circular heater shapes are morphed into single serpentine shape (see Fig. 15) into which insulated nichrome wires are inserted to electrically heat the main and guard heaters. Thermocouple holes of 1 mm diameter with varying depths are provided radially along the heaters into which K-type thermocouples (Omega TT-K-36) are inserted to measure the hot side temperature of the sample. The engineering drawings of main and guard heaters are given in Appendix (7.1).

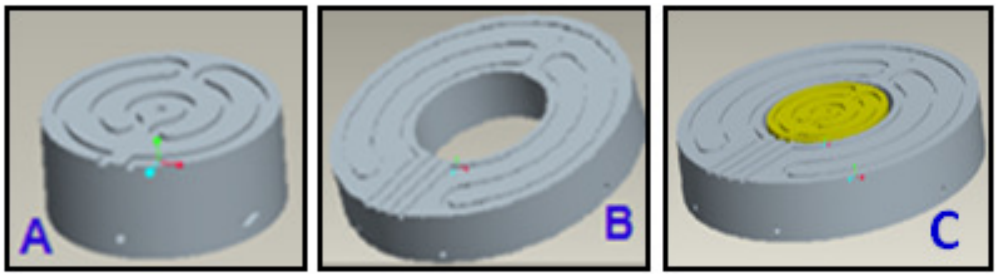

Figure 15: Pro-E drawing of (a) Main heater design, (b) Guard heater design, (c) Heater assembly.

Table 3: Dimensions of Main Heater, Guard Heater and Cold Plate.

Heater	Dimensions (mm)
Main Heater	Diameter : 24
	Height : 10
Guard Heater	Outside Diameter : 60
	Inside Diameter : 26
	Height : 10
Cold Plate	Diameter : 60
	Height : 15

3.1.1.2 Cold Plate Design

The cold plates are used to maintain the cold side of the sample at a constant temperature. The material used for the cold plate is copper and is designed to be a two pass coolant passage system (see Fig. 16). The dimensions of cold plate used are as given in Table 3. Temperature measurement of the cold plate at different radial locations is done by inserting K-type (Omega TT-K-36) thermocouples into the 1 mm diameter thermocouple holes as shown in Fig. 16. The dimensioned drawing of the cold plate is included in Appendix (7.1).

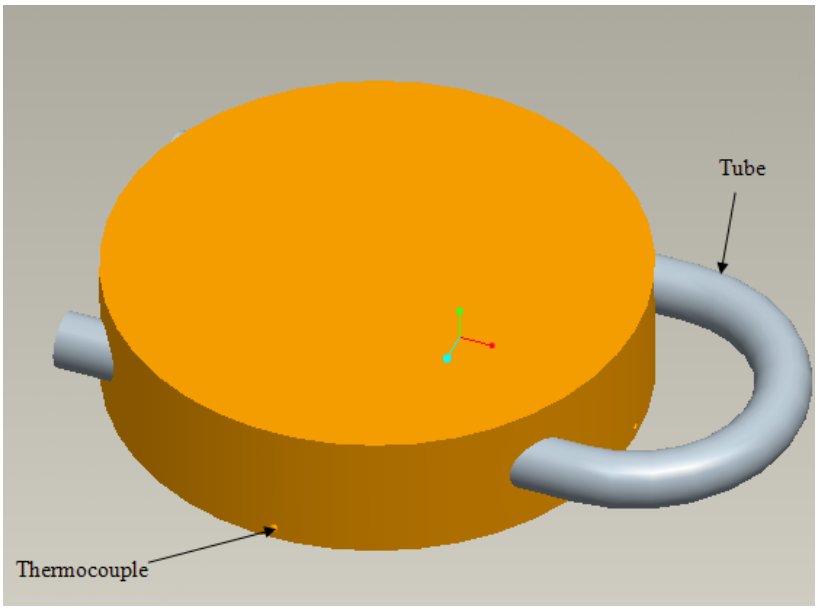

Figure 16: Pro-E drawing of cold plate.

3.1.1.3. Loading system

The loading system consists of

1. Loading clamp
2. Load cell

The assembly of heaters, samples and cold plates (see Fig. 14) is compressed to a required pressure by using the loading clamp. A portable arbor press is used which is bolted on to the workbench and has a maximum capacity of 3 tons.

The load cell placed between the loading clamp and the cold plate is used to measure the applied compressive force. Omega LC304-5K model load cell is used for the load measurement. It can measure loads up to 5000 lb. The transducer is factory calibrated and

the calibration chart is as shown in Table 4. The calibration data was verified by placing, and then recording known weights on the load cell before being used for the experiments.

Table 4: Load cell calibration data provided by manufacturer.

Force (lb)	Unit Data (mVdc)
0.00	0.0000
2500.00	10.3055
5000.00	20.5435
2500.00	10.2916
0.00	-0.0014

3.1.2. Constant Temperature Bath

The temperature bath used for the experiments is LAUDA RCS series having a temperature range of 0 to 150°C and with water as the coolant. The constant temperature water from the bath is used to maintain the cold plates at a fixed temperature.

3.1.3. Power supply

Three power supplies are used for the experiments for

1. Main heater
2. Guard heater
3. Load cell

Model DIGI 35A power supplies by Electro industries are used for the main and guard heaters while Model 303D is used to provide the required excitation voltage for the load cell. The current and voltage values from the power supply are manually recorded for each experiment.

3.1.4. Data Acquisition

The entire system was monitored using a high speed National instruments brand Data Acquisition system (DAQ). NI-SCXI model hardware is used to acquire the data and is controlled using LabVIEW 8.2 software. The front panel of LabVIEW is as shown in Fig. 17.

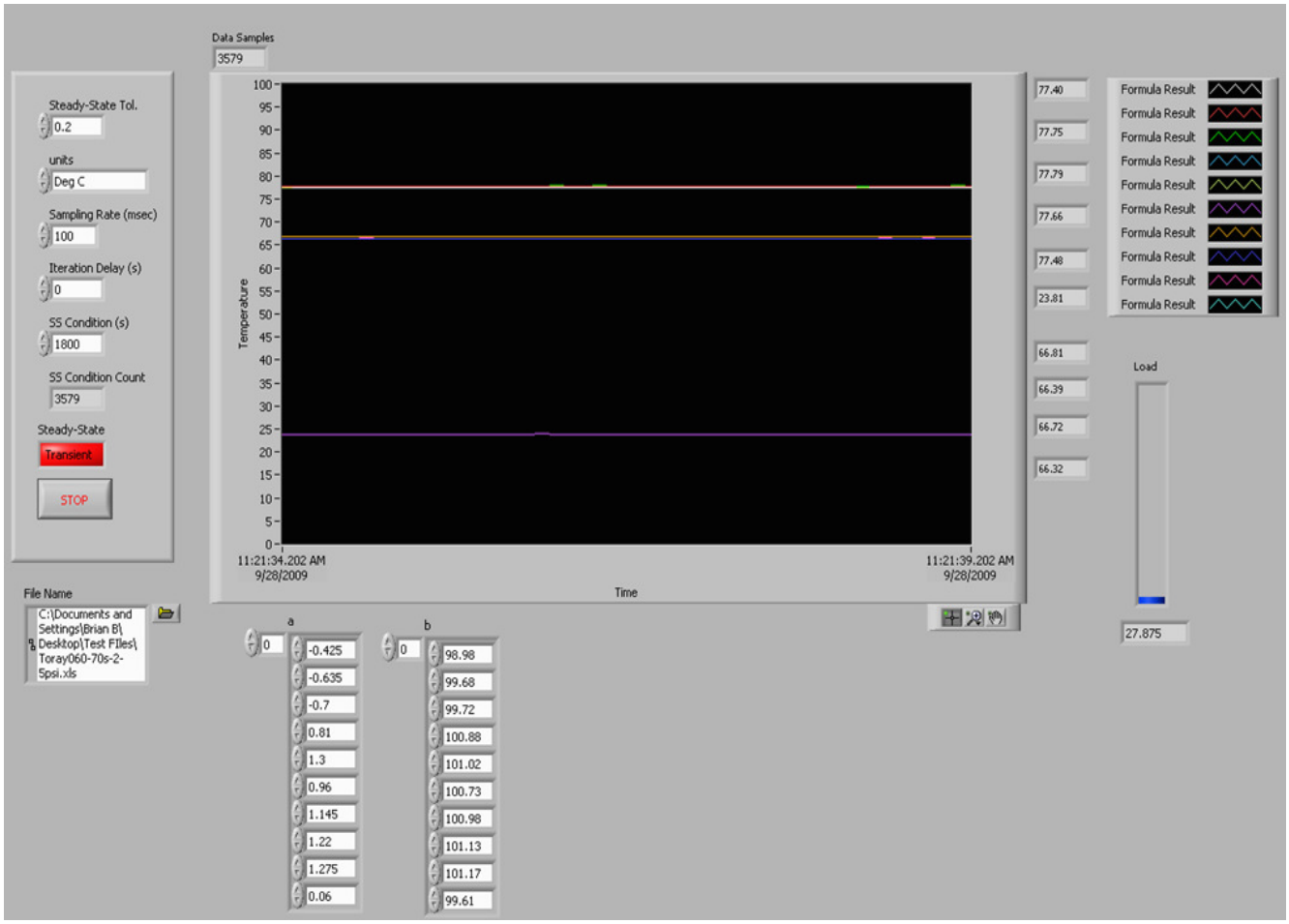

Figure 17: Front panel view of LabVIEW used for data acquisition.

Thermocouples are placed on heaters as well as the cold plates at various locations radially to measure the hot side and cold side temperatures of the sample, respectively. Ultra thin K-type (Omega TT-K-36) thermocouples of size 22 AWG are used for temperature measurement. Thermocouples inserted into the main and guard heaters are monitored to ensure that both heaters are at the same temperature. Thermocouples are calibrated using a two point calibration scheme. Ice point and steam point of water are used as the two fixed points. Melting ice in water constituted an ice point where the temperature of water is 0°C. The thermocouple is inserted into the ice bath and the reading is recorded. The thermocouple is then inserted into a steam bath which is nothing but water boiling where the water temperature is 100°C and the corresponding thermocouple temperature is recorded. The temperature is corrected to take the actual reading by using a correction formula given by Eqn. (22).

$$T = a * \tau + b \tag{21}$$

$$T = \left[\frac{T_{steam} - T_{ice}}{\tau_{steam} - \tau_{ice}}\right] * \tau + \left[T_{ice} - \left(\frac{T_{steam} - T_{ice}}{\tau_{steam} - \tau_{ice}}\right) * \tau_{ice}\right] \tag{22}$$

where, T is the correct temperature and τ is the uncorrected temperature as read by the DAQ system. The correction is based on ice point and is of linear form. The resulting accuracy of thermocouple is ±0.1°C. The correction formula is programmed into LabVIEW as to write the corrected temperature reading into the data file.

3.2. Experimental Procedure and Data Reduction

3.2.1. GDL Thickness Measurement

GDL thickness measurement is important to determine the actual thermal conductivity of the GDL sample at a given compression. The thickness measurement was carried out using the same test section that is used for thermal conductivity measurement by using a digital microscope (Keyence VHX-500). Figure 18 shows the test section used for GDL thickness measurement.

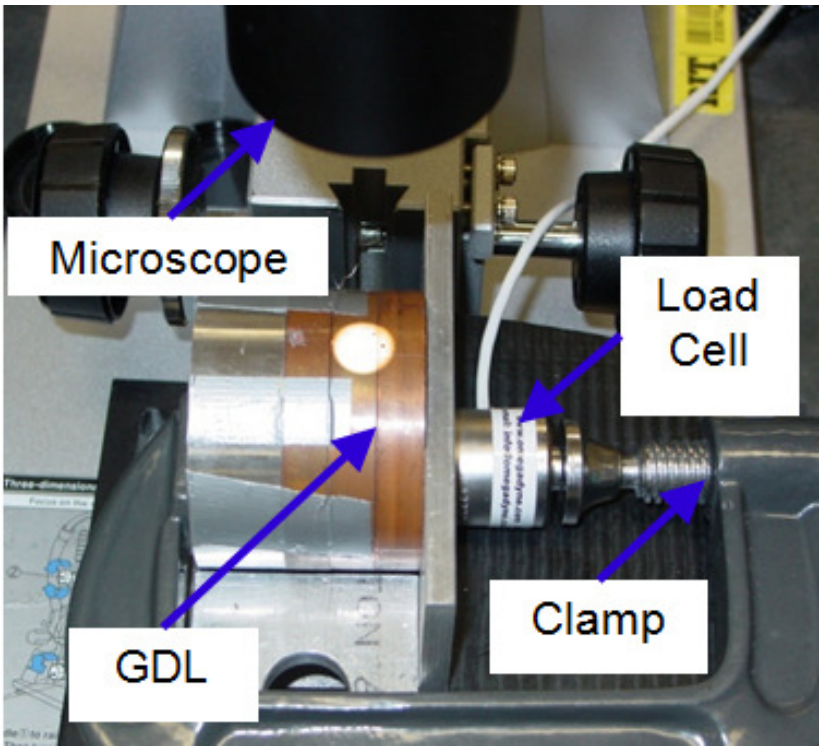

Figure 18: Test section used for GDL thickness measurement.

A relative method was used to calculate the GDL thickness for different compressions. Figures 19 (a) and (b) depict the principle used to measure uncompressed and compressed GDL thicknesses, respectively. In both the cases, the sample is placed between two copper pieces, i.e., the heater and cold plate.

In compressed GDL thickness measurement, GDL sample is compressed between the copper pieces where the lower piece is stationary and the upper piece is compressed. The applied load is measured using the load cell, and the GDL thickness for a particular compression is calculated using Eqn. (24).

$$L = L_2 - (L_1 - L_{known}) \tag{23}$$

$$L_c = L - (L_2 - L_3) \tag{24}$$

where, L is the uncompressed GDL thickness, L_c is the compressed GDL thickness, L_{known} is the known plastic thickness. In these GDL thickness measurements, the distance between the references is measured at two diametrically opposite locations and the obtained values are averaged.

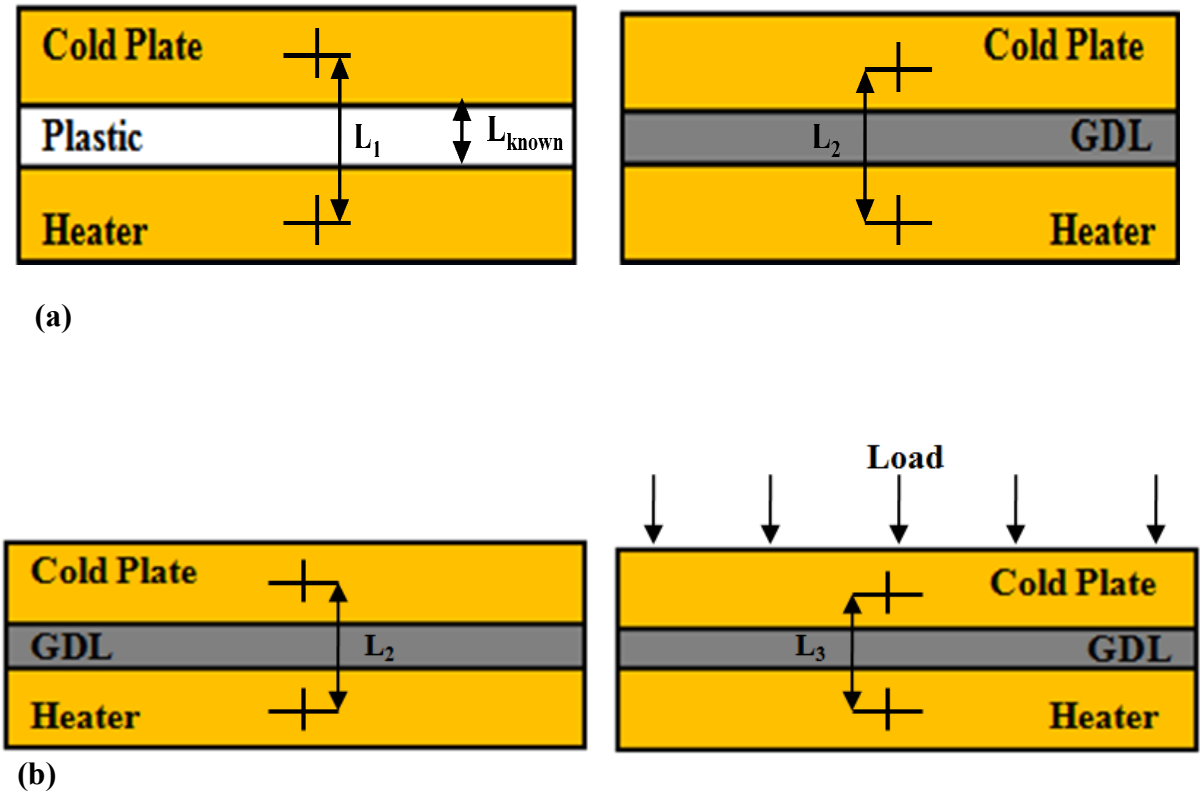

Figure 19: (a) Principle of GDL thickness measurement, (b) Principle of compressed GDL thickness measurement.

3.2.2. Thermal Conductivity Measurement

Two identical GDL samples whose thermal conductivity is to be measured are placed on either side of the heater and are compressed using the cold plates as shown in Fig. 20. The experiments are carried out for two thicknesses of the same sample to eliminate the contact resistance term.

During the experiment, the constant temperature bath is turned on as to maintain the cold plate at a fixed temperature while the power supply is used to heat the main heater so that a

temperature drop is produced across the sample. The guard heater is maintained at the same temperature as that of the main heater by adjusting the guard heater power supply. The temperature drop across the sample is monitored using the LabView software. Once the temperature bath reaches a constant temperature, the entire heater - sample - cold plate assembly is compressed by using the loading clamp and the compressed load measured by the load cell is monitored using LabVIEW. The compressed sample is then allowed to reach a steady state which is nothing but a temperature fluctuation within 0.2°C for a period of 30 minutes. As the steady state is reached, LabVIEW records and writes the hot side and cold side temperatures of the sample, and the applied load reading on to an excel sheet. The same procedure is repeated for the second thickness at the same compression, and these data are then used to calculate the thermal conductivity of GDL as described below.

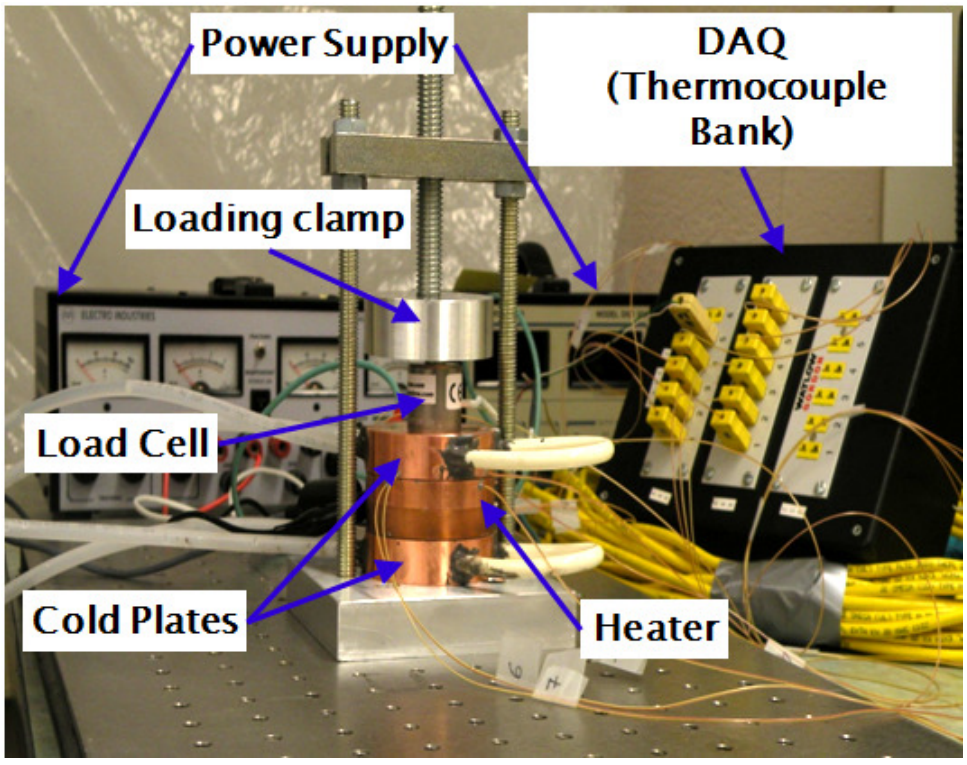

Figure 20: Test section used for thermal conductivity measurement.

The total resistance to the heat flow through the sample which is the sum of thermal resistance and contact resistance can be expressed using Fourier equation as:

$$R_{Total} = \frac{\Delta T}{\left(Q/_2\right)} = R_{th} + R_{CR} \tag{25}$$

where, R_{Total} is the total resistance to heat flow through the sample, R_{th} is the sample thermal resistance, R_{CR} is the contact resistance between the sample and copper, ΔT is the temperature drop across the sample, and Q is the heat transferred through the sample which is given by:

$$Q = V * I \tag{26}$$

The thermal resistance offered by the sample is given by:

$$R_{th} = \frac{L}{k\,A} \tag{27}$$

where, L is the thickness of the sample, k is the thermal conductivity, and A is the heat transfer area.

For two thicknesses of the sample under same compression, the contact resistance between the sample and the copper surface is assumed to be a constant. Using equations (25) and (27) for two different sample thicknesses and then simplifying them gives the thermal conductivity of the sample:

$$k = \frac{L_1 - L_2}{(R_{Total1} - R_{Total2})\,A} \tag{28}$$

where, L_1 and L_2 are the two sample thicknesses.

Thermal conductivity measurement in the present work is performed for two commercially available GDL samples – Toray and SGL. Thermal conductivity of Toray was performed using two samples of different thickness namely, Toray-060 and Toray-120. In case of SGL, SGL-25BC and SGL-35BC were used for the measurements. The tests were carried out for different temperatures by keeping a constant compression of 0.04 MPa while thermal conductivity measurement as a function of compression was performed at a constant temperature of 58°C.

3.2.3. Uncertainty Analysis

The uncertainty in the experimental results is discussed in the following section. Uncertainty is of the form given by Eqn. (29).

$$U = \sqrt{B^2 + P^2} \tag{29}$$

where, U is the uncertainty, B is the Bias error and P is the Precision error. Bias error is one which causes the values to be different from the true value and precision error is that which is generated by random values.

In order to estimate the uncertainty in the experimental results obtained, the accuracy of the measurement instruments must be known first. The temperature reading from thermocouples has an accuracy of ±0.1°C. The bias errors are based upon these measured accuracies. The bias error is the accuracy of the measurement divided by a typical reading. Equation (30) gives the bias error for voltage.

$$B_V = \frac{\Delta V}{V} \tag{30}$$

3.2.3.1. Uncertainty in Heat Applied

Heat is applied to the sample electrically heating the insulated nichrome wires by using the power supply as explained in section (3.1.3) and the heat applied is given by:

$$Q = V\ I \tag{31}$$

The uncertainty for the heat applied can be determined by calculating the Bias error and precision error which are given by the following equations.

$$B_Q = \sqrt{\left(\frac{\partial Q}{\partial V}\ B_V\right)^2 + \left(\frac{\partial Q}{\partial I}\ B_I\right)^2} \tag{32}$$

where, B_Q is the bias error for the heat applied, B_V is the bias error for the voltage supplied, B_I is the bias error for the current applied.

$$P_Q = 1.96\sqrt{\left(\frac{\partial Q}{\partial V}\ \sigma_V\right)^2 + \left(\frac{\partial Q}{\partial I}\ \sigma_I\right)^2} \tag{33}$$

where, P_Q is the precision error for the heat applied, σ_V is the standard deviation for the voltage supplied, σ_I is the standard deviation for the current applied. The uncertainty in the heat applied (Q) is then calculated as:

$$U_Q = \sqrt{B_Q^2 + P_Q^2} \tag{34}$$

3.2.3.2. Uncertainty in Thermal Conductivity

Thermal conductivity is determined by using the following equation:

$$k = \frac{L_1 - L_2}{(R_{Total1} - R_{Total2})\ A} \tag{35}$$

where, L_1, L_2 are the two thicknesses, $R_{Total1}$is the total resistance corresponding to thicknesses L_1, R_{Total2} is the total resistance corresponding to thickness L_2, A is the heat

transfer area. Before calculating the uncertainty involved in the thermal conductivity, uncertainty in the heat transfer area (A) is calculated. The heat transfer area is given by:

$$A = \frac{\pi}{4} D^2 \tag{36}$$

where, D is the diameter of the main heater. The Bias error can be calculated as:

$$B_A = \sqrt{\left(\frac{\partial A}{\partial D}\, B_D\right)^2} \tag{37}$$

where, B_D is the bias error for the measured diameter. The precision error is given by:

$$P_A = 1.96 \sqrt{\left(\frac{\partial A}{\partial D}\, \sigma_D\right)^2} \tag{38}$$

Where, σ_D is the standard deviation for the main heater diameter. The uncertainty in heat transfer area (A) is then calculated as:

$$U_A = \sqrt{B_A^2 + P_A^2} \tag{39}$$

The uncertainty in thermal conductivity (k) is then calculated as:

Bias error:

$$B_k = \sqrt{\left(\frac{\partial k}{\partial A}\, B_A\right)^2 + \left(\frac{\partial k}{\partial \Delta L}\, B_{\Delta L}\right)^2 + \left(\frac{\partial k}{\partial R_{Total}}\, B_{R_{Total}}\right)^2} \tag{40}$$

where, B_A is the bias error for heat transfer area, $B_{\Delta L}$ is the bias error for difference in thickness between the two samples, B_{RTotal} is the bias error for total resistance.

Precision error:

$$P_k = 1.96 \sqrt{\left(\frac{\partial k}{\partial A}\, \sigma_A\right)^2 + \left(\frac{\partial k}{\partial \Delta L}\, \sigma_{\Delta L}\right)^2 + \left(\frac{\partial k}{\partial R_{Total}}\, \sigma_{R_{Total}}\right)^2} \tag{41}$$

Where, σ_A is the standard deviation for heat transfer area, $\sigma_{\Delta L}$ is the standard deviation for difference in thickness between the two samples, σ_{RTotal} is the standard deviation for total resistance.

Uncertainty in thermal conductivity (k):

$$U_k = \sqrt{B_k^2 + P_k^2} \tag{42}$$

The resulting uncertainties are presented. The resulting uncertainty for Toray GDL is 8.77% and SGL is 6.06%.

3.2.3.3. Uncertainty in Unit Area thermal Resistance

Unit area thermal resistance is given by the equation:

$$R^{"} = \frac{L}{k} \tag{43}$$

where, L is the thickness of the sample and k is the thermal conductivity. to determine the uncertainty in R", the uncertainty in the thickness is calculated.

Bias error:

$$B_{R^{"}} = \sqrt{\left(\frac{\partial R^{"}}{\partial L}\, B_L\right)^2 + \left(\frac{\partial R^{"}}{\partial k}\, B_k\right)^2} \tag{44}$$

where, B_L is the bias error for sample thickness, B_k is the bias error for thermal conductivity.

Precision error:

$$P_{R^{"}} = 1.96\sqrt{\left(\frac{\partial R^{"}}{\partial L}\, \sigma_L\right)^2 + \left(\frac{\partial R^{"}}{\partial k}\, \sigma_k\right)^2} \tag{45}$$

Where, σ_L is the standard deviation for sample thickness, σ_k is the standard deviation for thermal conductivity.

Uncertainty in unit area thermal resistance ($R^{"}$):

$$U_{R^{"}} = \sqrt{B_{R^{"}}^2 + P_{R^{"}}^2} \tag{46}$$

The uncertainty in unit area thermal resistance for Toray-060, Toray-120, SGL-25BC and SGL-35BC are 9.54%, 8.92%, 7.07% and 6.53% respectively.

3.2.3.4. Uncertainty in Contact Resistance

The contact resistance between the sample and the copper surface is back calculated from the thermal conductivity equation which is given by:

$$R_{CR} = \frac{\left(R_{Total1} - \left(\frac{L_1}{k\,A}\right)\right)}{2} A \tag{47}$$

where, R_{Total1} is the total resistance to heat flow for the sample with thickness L_1, k is the thermal conductivity of the sample, A is the heat transfer area. The uncertainty involved with the contact resistance is calculated using the following equations.

Bias error:

$$B_{R_{CR}} = \sqrt{\left(\frac{\partial R_{CR}}{\partial R_{Total}}\, B_{R_{Total}}\right)^2 + \left(\frac{\partial R_{CR}}{\partial L}\, B_L\right)^2 + \left(\frac{\partial R_{CR}}{\partial k}\, B_k\right)^2 + \left(\frac{\partial R_{CR}}{\partial A}\, B_A\right)^2} \tag{48}$$

where, B_{RTotal} is the bias error for total resistance, B_L is the bias error for sample thickness, B_k is the bias error for thermal conductivity, B_A is the bias error for heat transfer area.

Precision error:

$$P_{R_{CR}} = 1.96\sqrt{\left(\frac{\partial R_{CR}}{\partial R_{Total}}\, \sigma_{R_{Total}}\right)^2 + \left(\frac{\partial R_{CR}}{\partial L}\, \sigma_L\right)^2 + \left(\frac{\partial R_{CR}}{\partial k}\, \sigma_k\right)^2 + \left(\frac{\partial R_{CR}}{\partial A}\, \sigma_A\right)^2} \tag{49}$$

where, σ_{RTotal} is the standard deviation for total resistance, σ_L is the standard deviation for sample thickness, σ_k is the standard deviation for thermal conductivity, σ_A is the standard deviation for heat transfer area.

Uncertainty in contact resistance (R_{CR}):

$$U_{R_{CR}} = \sqrt{B_{R_{CR}}^2 + P_{R_{CR}}^2} \tag{50}$$

The uncertainty in contact resistance for Toray is 10.73% and SGL is 8.87%.

4. RESULTS AND DISCUSSION

This chapter discusses in detail the results obtained from the thermal conductivity measurements performed on two commercially available GDL samples namely, Toray and SGL. Toray-060 and Toray-120 were used as the samples having two different thicknesses for thermal conductivity measurement of Toray while SGL-25BC and SGL-35BC were used in the case of SGL. First, the GDL thickness measurement was performed as a function of compression on each of the GDL samples and later GDL thermal conductivity measurements were then carried out for different temperatures and compressions.

4.1. GDL Thickness Measurement under Compression

Gas Diffusion Layer (GDL) thickness at a given compression is critical in determining the thermal conductivity of GDL. The thickness of GDL as a function of compression was measured using the methodology as explained in section (3.2.1). Figure 21 represents the graph of GDL thickness versus compression for Toray-060, Toray-120, SGL-25BC and SGL-35BC samples.

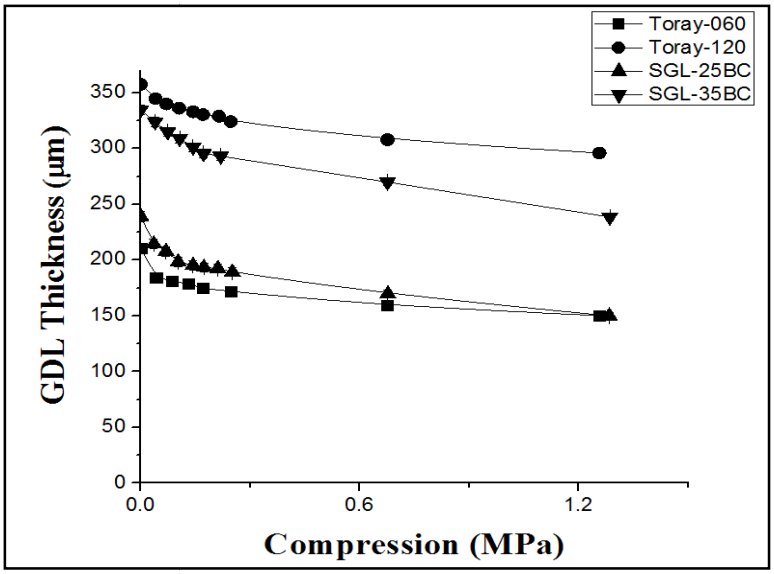

Figure 21: Plot of GDL thickness versus compression for Toray-060, Toray-120, SGL-25BC and SGL-35BC GDL samples.

The linear section of the plot was extrapolated to zero compression to obtain the GDL thickness at zero load as schematically represented in Fig. 22. Table 5 shows the thickness of GDL at zero load reported by the manufacturer and that obtained in the current work by the extrapolation method.

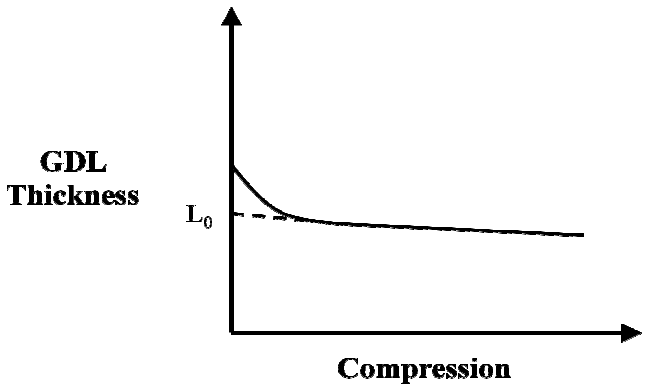

Figure 22: Schematic of thickness versus compression plot to calculate GDL thickness at zero load.

Table 5: GDL thickness at zero load

Sample	Thickness at zero load reported by manufacturer (μm)	Thickness at zero load obtained in current work (μm)
Toray-060	190	171.2±3
Toray-120	370	332.7±3
SGL-25BC	235	194.2±3
SGL-35BC	325	303.8±3

By using the compressed GDL thickness and GDL thickness at zero load, two thermal conductivities are calculated from the experimental data:

1. Actual thermal conductivity:

$$k_{actual} = \frac{(L_{c1} - L_{c2})}{(R_{Total1} - R_{Total2})A} \tag{51}$$

where, L_{c1}, L_{c2} are compressed GDL thicknesses.

2. Apparent thermal conductivity

$$k_{apparent} = \frac{(L_{01} - L_{02})}{(R_{Total1} - R_{Total2})A} \tag{52}$$

where, L_{01}, L_{02} are GDL thicknesses at zero load.

4.2. Thermal Conductivity Measurement

4.2.1. Validation of Test section

The validation of the methodology is critical before performing the actual GDL thermal conductivity measurement. Hence PTFE sheets of known thermal conductivity and having two different thicknesses were used. The two thicknesses used were 127 μm and 254 μm and the tests were performed at room temperature (~26°C) and the uncertainty involved was estimated to be 8.5%. Table 6 shows the comparison of thermal conductivity measured for PTFE sheets by using the current methodology and that reported in literature.

Table 6: Comparison of Thermal Conductivity of PTFE sheet with published values at 26°C

Measured Thermal Conductivity (Current Work) W/m-K	Hue et al. (2007) W/m-K	Jen et al. (1979) W/m-K
0.329	0.32	0.33

4.2.2. GDL Thermal conductivity

Before performing the GDL thermal conductivity measurements, repeatability tests were performed on each of the GDL samples in order to ascertain the reliability of the obtained results. The tests were repeated three times for each GDL sample.

The procedure used for measuring the thermal conductivity of GDL is explained in detail in section (3.2.2). For instance, at a compression of 0.17 MPa the thickness for Toray-060 and Toray-120 were measured to be 174.8 μm and 330.4 μm respectively. The heat transfer area is the main heater area which was 4.475×10^{-4} m^2. The total resistances for Toray-060 and Toray-120 samples are calculated from Eqn. (25) and were determined to be 1.191 K/W and 1.405 K/W respectively at a compression of 0.17 MPa and temperature of 58°C. These values are then used in Eqn. (28) to determine the thermal conductivity of Toray sample which was found to be 1.626 W/m-K.

Figure 23 shows the plot of thermal conductivity versus Temperature for Toray and SGL GDLs at 0.04 MPa compression. It was observed that the thermal conductivity of Toray decreased with temperature. Khandelwal et al. [12] explained this behavior of Toray to be due to the presence of carbonized thermo-setting resins present. Thermal conductivity of this thermo-setting resin which acts as the binder in Toray decreases as temperature increases [12, 20]. Also, it was found that the thermal conductivity of SGL GDL to be almost constant with temperature.

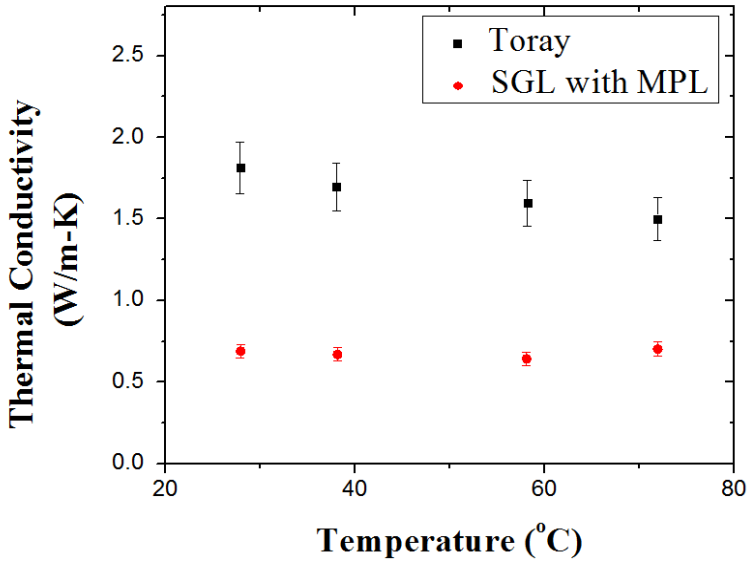

Figure 23: Plot of Thermal conductivity versus Temperature for Toray and SGL GDL samples at 0.04 MPa compression.

Thermal conductivities of Toray and SGL GDLs are plotted as a function of compression as shown in Fig. 24. It was found that the thermal conductivities of both Toray and SGL increased with compression. When under a clamping force, the carbon fibers in the GDL get compressed leading to a reduction in the pore space. This reduction in the porosity results in an increased GDL thermal conductivity. The plot also shows the apparent thermal conductivity against compression. It was observed that the apparent thermal conductivity values were higher than the actual thermal conductivity. This reinforces that the GDL thickness variation under compression is to be considered while measuring the thermal conductivity.

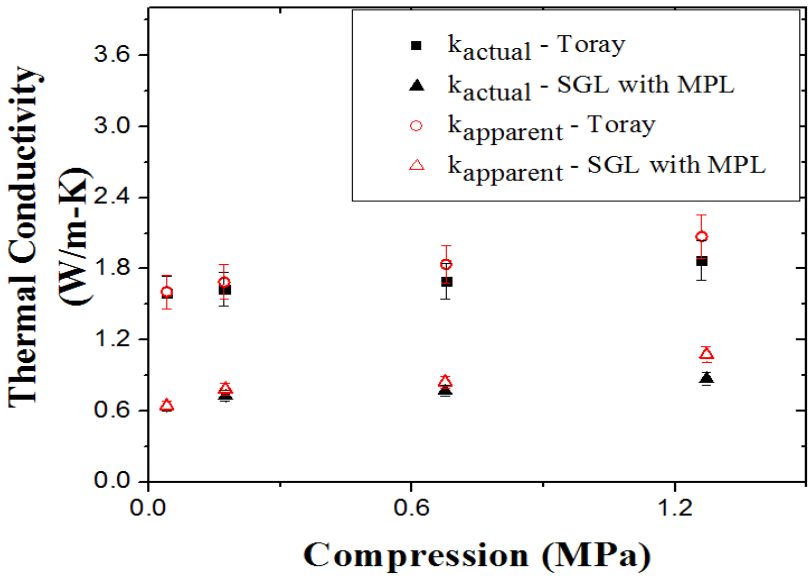

Figure 24: Thermal conductivity plot as a function of compression for Toray and SGL GDL samples at 58°C.

The thermal conductivity values obtained from the experiments are for dry GDL cases where the entire GDL pores are air filled. In an operational fuel cell, liquid water is also present in the GDL pores. However, these dry GDL thermal conductivity values could be used for modeling the start-up of the fuel cell. Moving forward experiments could be carried out to measure the thermal conductivity of GDL as a function of water saturation. Furthermore, due to the anisotropic nature of the GDL the in-plane thermal conductivity value will also be valuable.

4.2.3. Effective Thermal Conductivity (ETC) Model

The different effective thermal conductivity models reported in literature have been reviewed in section (2.5) and it was concluded that Krischer model which is a series-parallel

model, could be used to estimate the thermal conductivity of GDL by varying the distribution factor '*f*' for each of the GDL samples.

GDL is a highly porous material and gets deformed when compressed inside a fuel cell stack. It is assumed that the change in GDL volume under compression is merely due to reduction in the pore spaces not due to change in the carbon fiber volume. Porosity is defined as the ratio of pore volume to the total volume of the porous media.

$$\epsilon = \frac{V_p}{V_T} \tag{53}$$

where, V_p is the pore volume and V_T is the total volume of the porous media. When compressed, the porosity of the fibrous media can be derived in terms of the compression ratio and initial GDL porosity [21-22] which is given by the following equation:

$$\epsilon_c = \frac{V_{p,c}}{V_{T,c}} = \frac{V_0\epsilon_0 - V_0 CR}{(V_0 - V_0\, CR)} = \frac{\epsilon_0 - CR}{(1 - CR)} \tag{54}$$

where, ϵ_0 is the initial GDL porosity, ϵ_c is the compressed GDL porosity, $V_{p,c}$ is the compressed pore volume, $V_{p,T}$ is the compressed total volume, and *CR* is the compression ratio which is given by:

$$CR = \frac{L - L_c}{L} \tag{55}$$

where, L is the uncompressed GDL thickness and L_c is compressed GDL thickness.

At a compression of 0.17 MPa, the compression ratio (Eqn. (55)) for Toray-060 is 0.171. For this compression ratio of 0.171, the compressed porosity of Toray-060 at 0.17 MPa compression is calculated using Eqn. (54) and was found to be 0.73. For a distribution factor

f=0.0238, the thermal conductivity for Toray-060 is predicted using the Krischer model (Eqn. (16)) which was 1.63 W/m-K.

The plot showing the comparison of the actual thermal conductivity of Toray-060, toray-120, SGL-25BC and SGL-35BC with that estimated by the model is shown in Figs. 25, 26, 27 and 28 respectively.

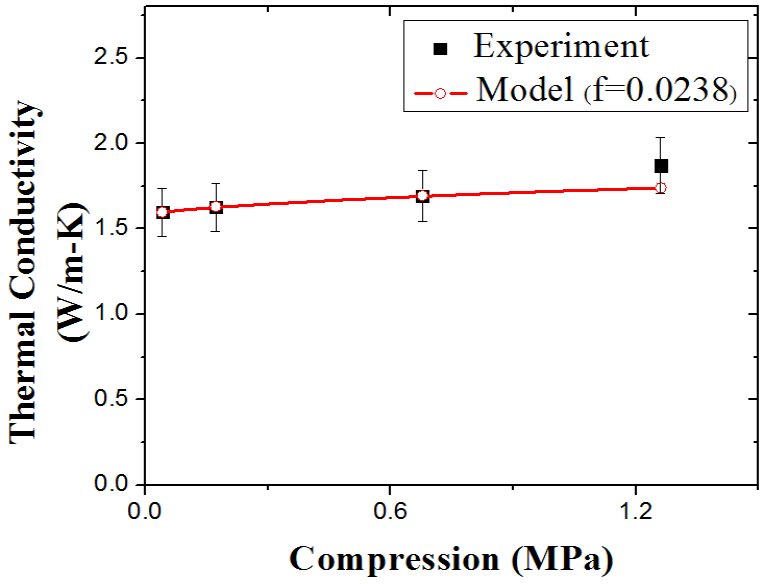

Figure 25: Comparison of experimental thermal conductivity with that predicted by the model for Toray-060.

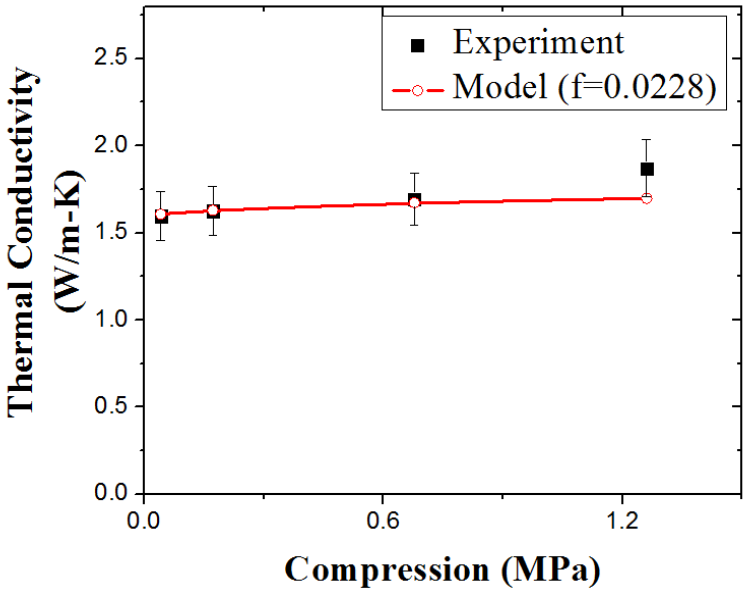

Figure 26: Comparison of experimental thermal conductivity with that predicted by the model for Toray-120.

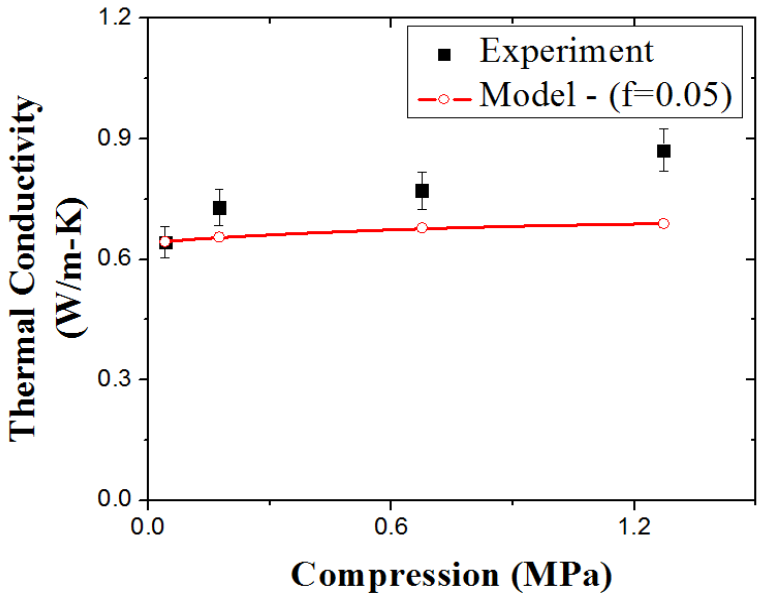

Figure 27: Comparison of experimental thermal conductivity with that predicted by the model for SGL-25BC.

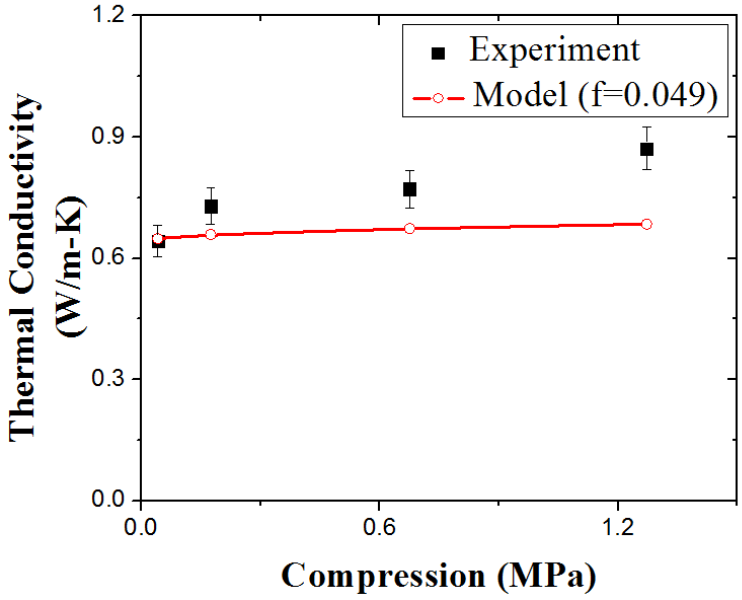

Figure 28: Comparison of experimental thermal conductivity with that predicted by the model for SGL-35BC.

The thermal conductivity values predicted by the model were found to closely match the experimentally determined thermal conductivity values for Toray-060 and Toray-120 samples.

However, slight variation was observed in case of SGL-25BC and SGL-35BC. This may due to the presence of Microporous Layer (MPL) on one side of SGL-25BC and SGL-35BC samples. MPL is a thin layer bonded onto catalyst layer side of the GDL and consists of carbon particles and 5-20 % of PTFE. It is a highly porous media with pore sizes in the range of 100-500 nm. In addition, the variation in the predicted value may be because of the fact that the model does not consider the PTFE content in SGL-25BC and SGL-35BC samples.

The model also does not consider the presence of PTFE and polymeric binder in the GDL. These constituents also contribute to the overall thermal conductivity of the GDL. For

instance the polymeric binder in case of Toray GDL causes the thermal conductivity of Toray to decrease with temperature.

Moreover, under compression in addition to the reduction in the pore volume the contact between the fibers become stronger causing the thermal conductivity to increase. This thermal conductivity increase due to better fiber contact is not considered by the model.

The detailed MATLAB codes used for the model to predict the thermal conductivity of Toray-060, Toray-120, SGL-25BC and SGL-35BC are provided in Appendix (7.2).

4.2.4. Area Thermal Resistance

Area thermal resistance is another parameter which could be used to define the thermal property of GDL samples. It is nothing but the thermal resistance offered by the GDL sample multiplied by the heat transfer area and is given by:

$$R'' = \frac{L}{k} \tag{56}$$

where, L is the thickness of the GDL sample and k is the thermal conductivity of GDL sample. Figure 29 shows the plot of area thermal resistance as a function of compression for Toray-060 and Toray-120. Figure 30 shows the plot of area thermal resistance as a function of compression for SGL-25BC and SGL-35BC. It was observed that the area thermal resistance for all GDL samples (Toray-060, Toray-120, SGL-25BC and SGL-35BC) to decrease with temperature. Furthermore, area thermal resistances of SGL series GDLs were higher than those for Toray series GDLs which is due to the lower thermal conductivity offered by the SGL series when compared to Toray.

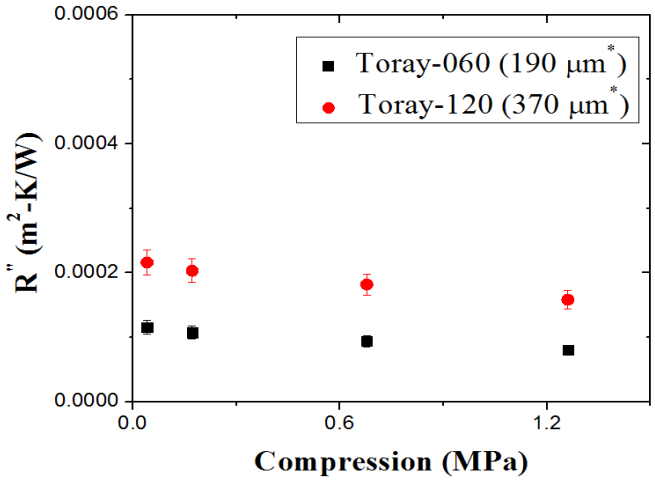

Figure 29: Area thermal resistance versus compression for Toray-060 and Toray-120.

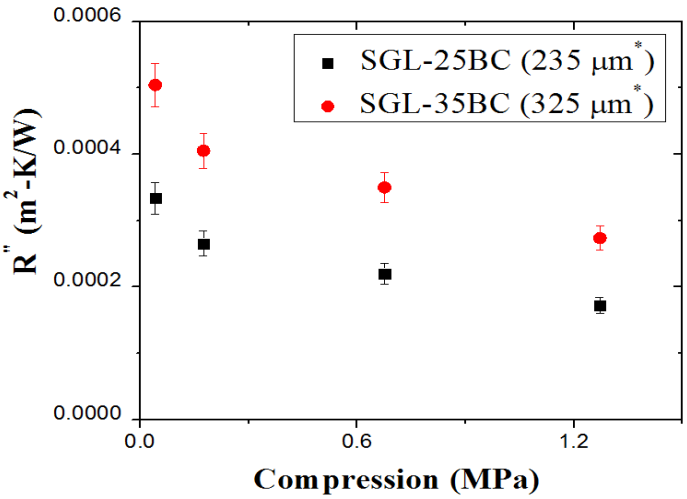

Figure 30: Area thermal resistance versus compression for SGL-25BC and SGL-35BC.

4.2.5. Contact Resistance

The contact resistance between the GDL surface and copper which was eliminated while calculating the thermal conductivity of GDL provides some critical information regarding the choice of materials for the bipolar plate. The contact resistance is different for different

GDL-bipolar material pair and the material. Contact resistance is calculated from the experimental data by using the following equation:

$$R_{CR} = \frac{\left(\left(\frac{\Delta T_1}{Q_1}\right) - \left(\frac{L_1}{k\,A}\right)\right)}{2} A \qquad (57)$$

where, R_{CR} is the contact resistance, L_1 is the thickness of sample, Q_1 is heat transfer rate corresponding to sample of thickness L_1, dT_1 is the temperature drop across the sample with thickness L_1, k is thermal conductivity of the sample, A is the heat transfer area. The factor 2 is used to determine the contact resistance of one GDL-copper pair.

Figure 31 shows the plot of contact resistance of GDL-copper pair as a function of compression for Toray and SGL GDLs.

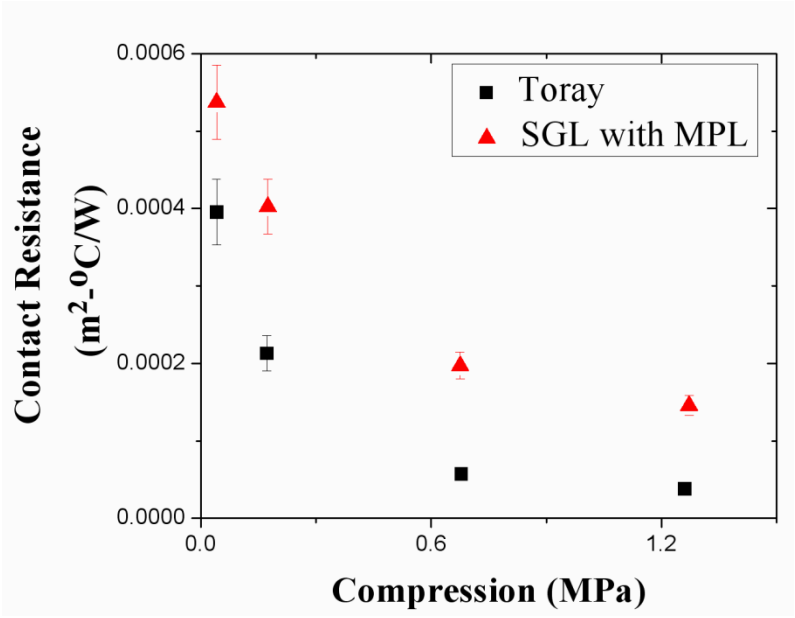

Figure 31: Plot of contact resistance of GDL-copper pair versus compression for Toray and SGL GDL samples.

The contact resistance for both the GDLs was found to decrease with compression. Furthermore, the contact resistance of SGL sample was found to be more when compared to that of Toray. This may be due to the fact that SGL sample has a microporous layer (MPL) on one of its sides. MPL has a granular structure which may cause a higher contact resistance. The electrical contact resistance of GDL with MPL is found to be higher than that for GDL without MPL [21]. Hence, applying the analogy between thermal and electrical properties, it can be said that thermal contact resistance of SGL is more than that of Toray.

5. CONCLUSIONS

An apparatus has been developed to measure the thermal conductivity of Gas Diffusion Layer (GDL) used in PEM fuel cell. Guarded hot plate method was used to perform the thermal conductivity experiments. During testing, two identical samples are sandwiched between the heater and cold plates. The contact resistance term is eliminated from the thermal conductivity term by using samples of two different thicknesses and also, by assuming that contact resistance at a given compression is a constant. The tests were performed to determine the thermal conductivity of Gas Diffusion Layer (GDL) as a function of temperature and compression and were carried out on two commercially available GDL samples – Toray and SGL. The following conclusions are drawn from the present work.

- Thickness of compressed GDL is critical in determining the actual thermal conductivity of the GDL at a given compression. GDL thickness at zero load is defined which is obtained by extrapolating the linear section of the GDL thickness versus compression plot. Apparent thermal conductivity calculated from GDL thickness at zero load was found to over predict the actual thermal conductivity values.
- Thermal conductivity tests for both the GDL samples were performed for different temperatures which correspond to the different operating conditions of the fuel cell. For Toray GDL thermal conductivity was found to decrease with temperature which may be due to the presence of the binder (carbonized thermo-setting resin) whose thermal conductivity decreases with temperature. However, the thermal conductivity of SGL was found to be constant with temperature.

- Thermal conductivities of both Toray and SGL samples were noted to increase with compression which is due to the reduction in the pore volume of the GDLs with compression.
- These dry thermal conductivity values measured could be used for start-up modeling in fuel cells.
- Krischer model developed to estimate thermal conductivity of GDL as a function of compression could predict values close to those obtained from the experiments. Slight variation in the results predicted by the model in case of SGL-25BC and SGL-35BC is observed due to the fact that the model does not take into account the presence of MPL on the GDL surface and also, due to the PTFE content in SGL.
- Area thermal resistance parameter was defined to understand clearly the thermal behavior of GDL and was observed to decrease with compression for all the GDL samples tested.
- The contact resistance between GDL-copper surfaces was noted to decrease with compression for both Toray and SGL sample. In addition, the contact resistance values of SGL were found to be larger than those for Toray.
- Moving forward the thermal conductivity measurement as a function of water saturation can be performed to understand the variation in the temperature distribution within the fuel cell stack under the actual operating condition.
- Moreover, due to the anisotropic behavior of the GDL in-plane GDL thermal conductivity measurement would be valuable for the thermal modeling of the fuel cell.

6.0. REFERENCES

[1] Mathias, M., Roth, J., Fleming, J., and Lehnert, W., 2003, *Handbook of Fuel Cells – Fundamentals, Technology and Applications,* John Wiley & sons, chap. 46.

[2] Bazylak, A., Sinton, D., Liu, Z.S., Djilali, N., 2006 " Effect of compression on liquid water transport and microstructure of PEMFC gas diffusion layers," Journal of Power Sources, Vol.163, pp. 784-792.

[3] Faghri, A. and Guo, Z., 2005, "Challenges and opportunities of thermal management issues related to fuel cell technology and modeling," International Journal of Heat and Mass Transfer, Vol. 48, pp. 3891-3920.

[4] Yu, S., and Jung, D., 2008, "Thermal management strategy for a proton exchange membrane fuel cell system with a large active cell area," Renewable Energy, Vol. 33, pp. 2540-2548.

[5] Ramousse, J., Didierjean, S., Lottin, O., and Maillet, D., 2008, "Estimation of the effective thermal conductivity of carbon felts used as PEMFC Gas Diffusion Layers," International Journal of Thermal Sciences, Vol. 47, pp. 1-6.

[6] Shi, Y., Xiao, J., Quan, S., Pan, M., and Yuan, R., 2008, "Fractal model for prediction of effective thermal conductivity of gas diffusion layer in proton exchange membrane fuel cell," Journal of Power Sources, Vol. 185, pp. 241-247.

[7] Flynn, D.R., Zarr, R.R., Hahn, M.M., and Healy, W.M., 2002, *Insulation Materials: Testing and Applications: 4th volume*, ASTM International, West Conshohocken, PA, pp. 98-115.

[8] Delan, A., Rennau, M., Schulz, S.E., and Gessner, T., 2003, "Thermal conductivity of ultra low-k dielectrics," Microelectronic Engineering, Vol. 70, pp. 280-284.

[9] Rodríguez-Pérez, M.A., Reglero, J.A., Lehmhus, D., Wichmann, M., de Saja, J.A., and Fernández, A., 2003, "The Transient Plane Source Technique (TPS) to measure thermal conductivity and its potential as a toll to detect in-homogeneities in metal foam," *International conference on Advanced Metallic Materials*, Smolenice, Slovakia, pp. 253-257.

[10] Burzo, M.G., Komarov, P.L., and Raad, P.E., 2006, "Optimized thermo-reflectance system for measuring the thermal properties of thin-films and their interfaces," *Semiconductor Thermal Measurement and Management Symposium, Twenty-Second Annual IEEE*, pp. 87-94.

[11] Vie, J.S., and Kjelstrup, S., 2004, "Thermal conductivities from temperature profiles in the polymer electrolyte fuel cell," Electrochimica Acta, Vol. 49, pp. 1069-1077.

[12] Khandelwal, M., and Mench, M.M., 2006, "Direct measurement of through-plane thermal conductivity and contact resistance in fuel cell materials," Journal of Power Sources, Vol. 161, pp. 1106-1115.

[13] Nitta, I., Himanen, O., and Mikkola, M., 2008, "Thermal conductivity and contact resistance of compressed gas diffusion layer of PEM fuel cell," Fuel Cells, Vol. 8, pp. 111-119.

[14] Carson, J.K., Lovatt, S.J., Tanner, D.J., and Cleland, A.C., 2005, "Thermal conductivity bounds for isotropic, porous materials," International Journal of Heat and Mass Transfer, Vol. 48, pp. 2150-2158.

[15] Carson, J.K., Lovatt, S.J., Tanner, D.J., and Cleland, A.C., 2006, "Predicting the effective thermal conductivity of unfrozen, porous foods," Journal of Food Engineering, Vol. 75, pp. 297-307.

[16] Jagjiwanram, R.S., 2004, "Effective thermal conductivity of highly porous two-phase systems," Applied Thermal Engineering, Vol. 24, pp. 2727-2735.

[17] Wang, J., Carson, J.K., North, M.F., and Cleland, D.J., 2006, "A new approach to modelling the effective thermal conductivity of heterogeneous materials," International Journal of Heat and Mass Transfer, Vol. 49, pp. 3075-3083.

[18] Wang, J., Carson, J.K., North, M.F., and Cleland, D.J., 2008, "A new structural model of effective thermal conductivity for heterogeneous materials with co-continuous phases," International Journal of Heat and Mass Transfer, Vol. 51, pp. 2389-2397.

[19] Sadeghi, E., Bahrami, M., and Djilali, N., 2008, "Analytic determination of the effective thermal conductivity of PEM fuel cell gas diffusion layers," Journal of Power Sources, Vol. 179: Elsevier, Amsterdam, 1000 AE, Netherlands, pp. 200-208.

[20] Bailleul, J.L., Guyonvarch, G., Garnier, B., Jarny, Y., Delaunay, D., 1996, " Identification of thermal properties of composite fiberglass / thermosetting resins: Application to the optimization of molding processes," Revue générale de thermique, Elsevier, Paris, France, Vol. 35, No. 409, pp. 65-77.

[21] Zhou, P., Wu, C.W., and Ma, G.J., 2006, "Contact resistance prediction and structure optimization of bipolar plates," Journal of Power Sources, Elsevier, Amsterdam, 1000 AE, Netherlands, Vol. 159, pp. 1115-1122.

[22] Chi, P.H., Chan, S.H., Weng, F.B., Su, A., Sui, P.C., and Djilali, N., 2009, "On the effects of non-uniform property distribution due to compression in the gas diffusion layer of PEMFC," International Journal of Hydrogen Energy, pp. 200-208.

7. APPENDIX

7.1. Appendix A: Test Section Drawings

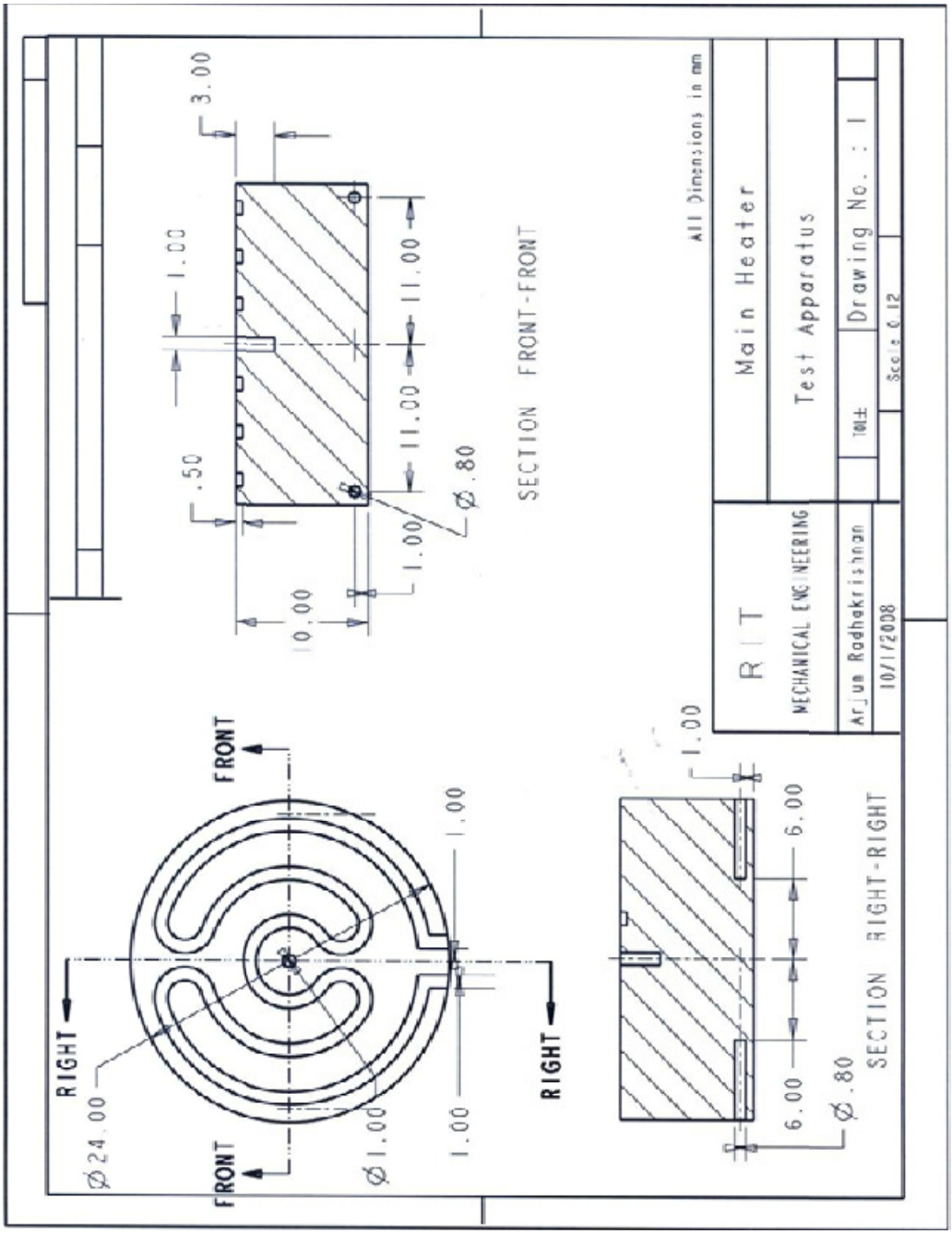

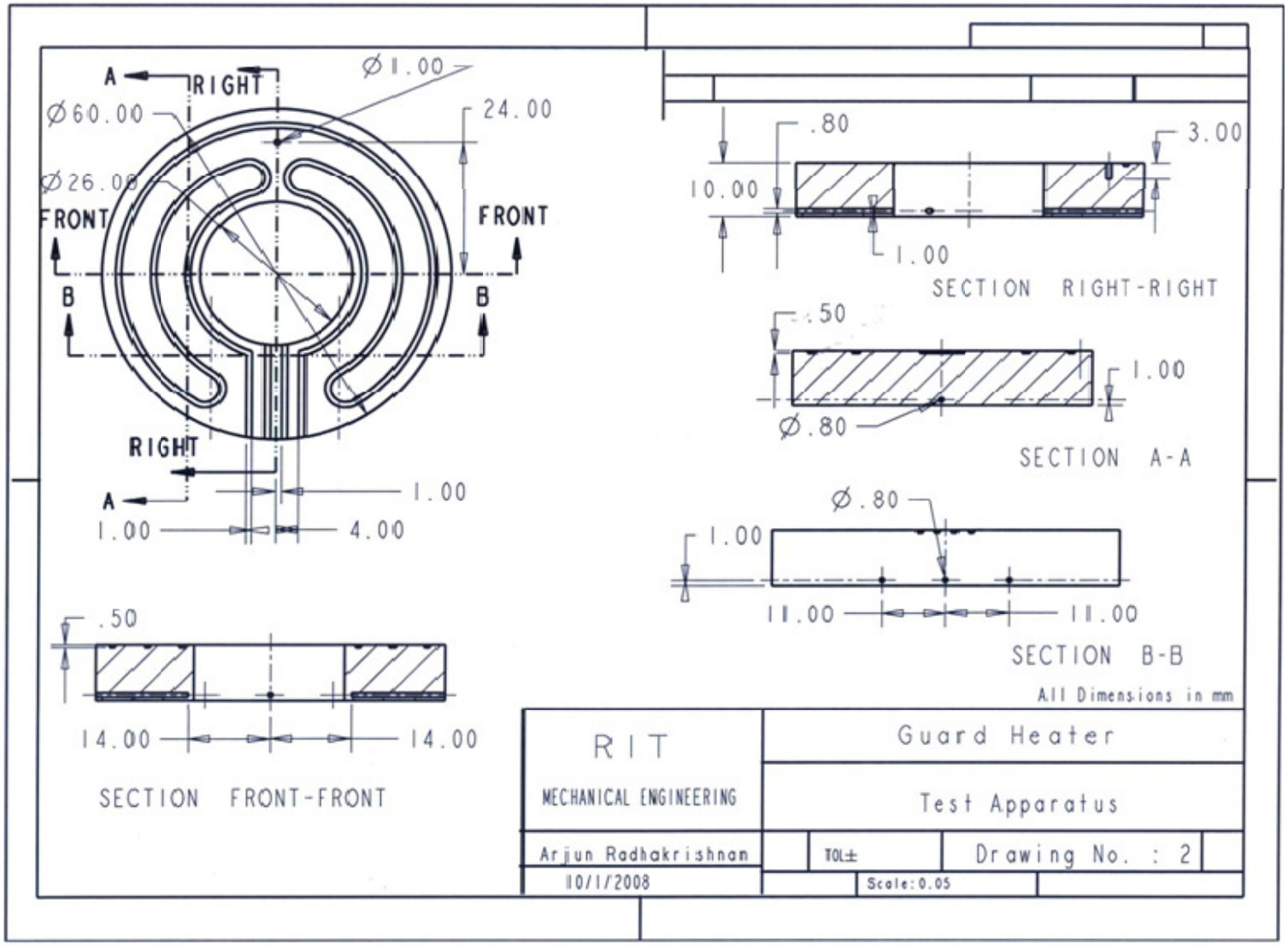
A
RIGHT
Ø60.00
Ø26.00
Ø1.00
24.00
FRONT
FRONT
B
B
RIGHT
A
1.00
1.00
4.00
.50
14.00
14.00
SECTION FRONT-FRONT
.80
3.00
10.00
1.00
SECTION RIGHT-RIGHT
.50
1.00
Ø.80
SECTION A-A
Ø.80
1.00
11.00
11.00
SECTION B-B
All Dimensions in mm
RIT
MECHANICAL ENGINEERING
Guard Heater
Test Apparatus
Arjun Radhakrishnan
10/1/2008
TOL±
Drawing No. : 2
Scale: 0.05

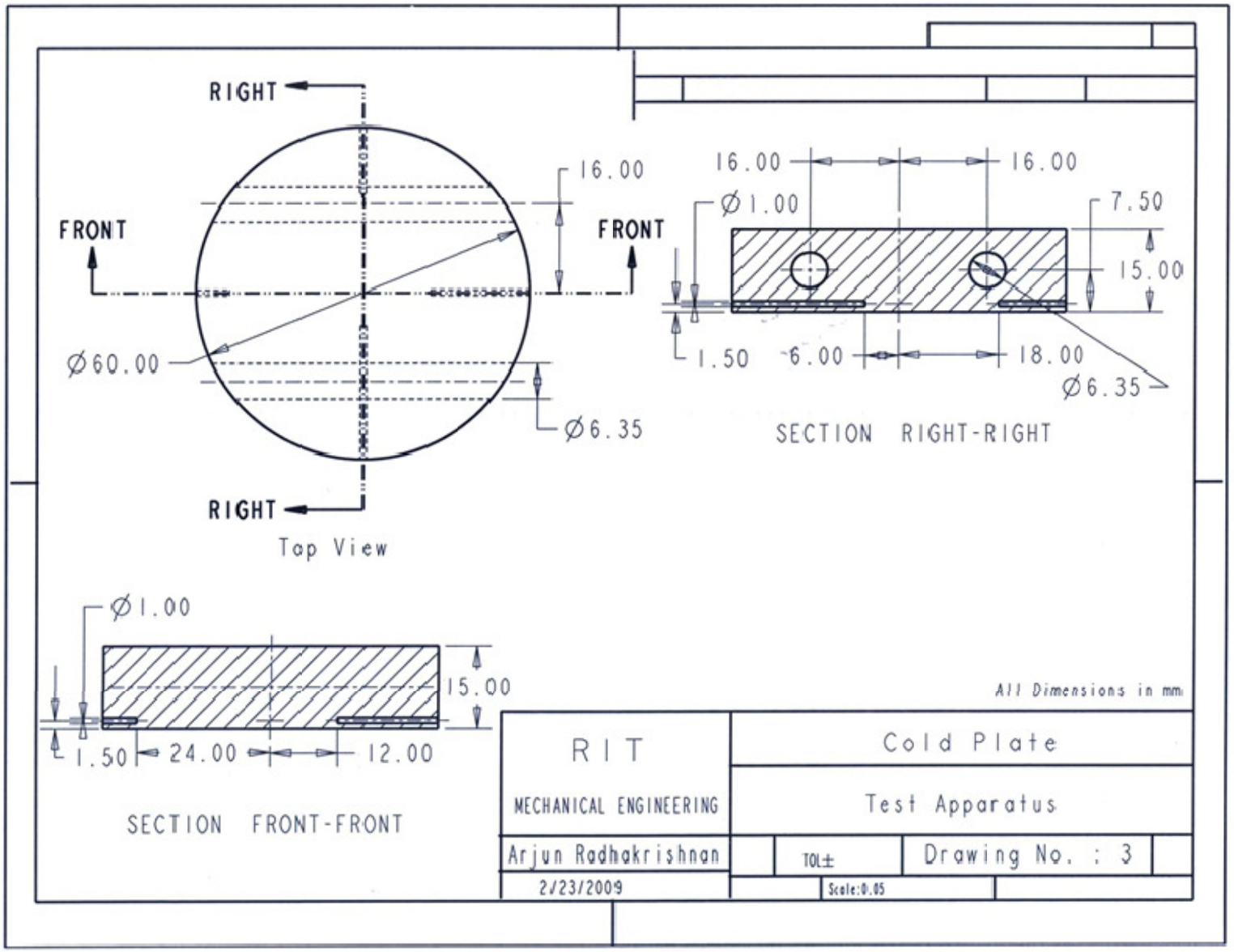
RIGHT
FRONT
FRONT
RIGHT
16.00
Ø60.00
Ø6.35
Top View
16.00
16.00
Ø1.00
7.50
15.00
1.50
6.00
18.00
Ø6.35
SECTION RIGHT-RIGHT
Ø1.00
15.00
1.50
24.00
12.00
SECTION FRONT-FRONT
All Dimensions in mm
RIT
MECHANICAL ENGINEERING
Arjun Radhakrishnan
2/23/2009
Cold Plate
Test Apparatus
TOL±
Drawing No. : 3
Scale:0.05

7.2. Appendix B: MATLAB Codes

7.2.1. Effective Thermal Conductivity Model for Toray-060

```
function Toray060TC()
E1=0.78;                                % Porosity
E2=1-E1;                                % Volume fraction of carbon fibers
k1=0.03;                                % Thermal conductivity of air
k2=120;                                 % Thermal conductivity of carbon fiber
Li=0.2109*10^-3;                        % Initial Thickness
Lc(1)=0.184125*10^-3;                   % Compressed Thickness @ 0.04 MPa
Lc(2)=0.174835*10^-3;                   % Compressed Thickness @ 0.17 MPa
Lc(3)=0.159165*10^-3;                   % Compressed Thickness @ 0.68 MPa
Lc(4)=0.15014*10^-3;                    % Compressed Thickness @ 1.26 MPa
for i=1:4
 dL(i)=Li-Lc(i);                        % Change in thickness
 CR(i)=dL(i)/Li;                        % Compression Ratio
 E(i)=((E1-CR(i))/(1-CR(i)));           % Porosity after compression
 kpar(i)=(E(i)*k1)+((1-E(i))*k2);       % Parallel model
 kser(i) =1/((E(i)/k1)+((1-E(i))/k2));  % Series model
 f=0.0238;                              % Distribution factor
 ktoray(i)=1/(((1-f)/kpar(i))+(f/kser(i))); % Krischer model
end
ktoray
end
```

7.2.2. Effective Thermal Conductivity Model for Toray-120

```
function Toray120TC()
E1=0.78;                                % Porosity
E2=1-E1;                                % Volume fraction of carbon fibers
k1=0.03;                                % Thermal conductivity of air
k2=120;                                 % Thermal conductivity of carbon fiber
Li=0.357435*10^-3;                      % Initial Thickness
Lc(1)=0.3447*10^-3;                     % Compressed Thickness @ 0.04 MPa
Lc(2)=0.330405*10^-3;                   % Compressed Thickness @ 0.17 MPa
Lc(3)=0.307885*10^-3;                   % Compressed Thickness @ 0.68 MPa
Lc(4)=0.295965*10^-3;                   % Compressed Thickness @ 1.26 MPa
for i=1:4
 dL(i)=Li-Lc(i);                        % Change in thickness
 CR(i)=dL(i)/Li;                        % Compression Ratio
 E(i)=((E1-CR(i))/(1-CR(i)));           % Porosity after compression
 kpar(i)=(E(i)*k1)+((1-E(i))*k2);       % Parallel model
 kser(i) =1/((E(i)/k1)+((1-E(i))/k2));  % Series model
 f=0.0228;                              % Distribution factor
 ktoray(i)=1/(((1-f)/kpar(i))+(f/kser(i))); % Krischer model
end
ktoray
end
```

7.2.3. Effective Thermal Conductivity Model for SGL-25BC

```
function SGL25BCTC()
E1=0.9;                                  % Porosity
E2=1-E1;                                 % Volume fraction of carbon fibers
k1=0.03;                                 % Thermal conductivity of air
k2=120;                                  % Thermal conductivity of carbon fiber
Li=0.23907*10^-3;                        % Initial Thickness
Lc(1)=0.21443*10^-3;                     % Compressed Thickness @ 0.04 MPa
Lc(2)=0.193525*10^-3;                    % Compressed Thickness @ 0.17 MPa
Lc(3)=0.161345*10^-3;                    % Compressed Thickness @ 0.67 MPa
Lc(4)=0.14984*10^-3;                     % Compressed Thickness @ 1.28 MPa
for i=1:4
 dL(i)=Li-Lc(i);                         % Change in length
 CR(i)=dL(i)/Li;                         % Compression ratio
 E(i)=((E1-CR(i))/(1-CR(i)));            % Porosity after compression
 kpar(i)=(E(i)*k1)+((1-E(i))*k2);        % Parallel model
 kser(i) =1/((E(i)/k1)+((1-E(i))/k2));   % Series model
 f=0.05;                                 % Distribution factor
 ksgl(i)=1/(((1-f)/kpar(i))+(f/kser(i))); % Krischer model
end
ksgl
end
```

7.2.4. Effective Thermal Conductivity Model for SGL-35BC

```
function SGL35BCTC()
E1=0.9;                                  % Porosity
E2=1-E1;                                 % Volume fraction of carbon fibers
k1=0.03;                                 % Thermal conductivity of air
k2=120;                                  % Thermal conductivity of carbon fiber
Li=0.334805*10^-3;                       % Initial Thickness
Lc(1)=0.32386*10^-3;                     % Compressed Thickness @ 0.04 MPa
Lc(2)=0.29544*10^-3;                     % Compressed Thickness @ 0.17 MPa
Lc(3)=0.260075*10^-3;                    % Compressed Thickness @ 0.67 MPa
Lc(4)=0.238495*10^-3;                    % Compressed Thickness @ 1.28 MPa
for i=1:4
 dL(i)=Li-Lc(i);                         % Change in thickness
 CR(i)=dL(i)/Li;                         % Compression Ratio
 E(i)=((E1-CR(i))/(1-CR(i)));            % Porosity after compression
 kpar(i)=(E(i)*k1)+((1-E(i))*k2);        % Parallel model
 kser(i) =1/((E(i)/k1)+((1-E(i))/k2));   % Series model
 f=0.049;                                % Distribution factor
 ksgl(i)=1/(((1-f)/kpar(i))+(f/kser(i))); % Krischer model
end
ksgl
end
```